International Journal of Mechanical Sciences 266 (2024) 108913

Contents lists available at ScienceDirect

International Journal of Mechanical Sciences

journal homepage: www.elsevier.com/locate/ijmecsci

A Dissolvable Micromechanics Model for Composites

S.K. Jalali [a,*], N.M. Pugno [a,b,*]

[a] Laboratory for Bio-Inspired, Bionic, Nano, Meta Materials & Mechanics, Department of Civil, Environmental and Mechanical Engineering, Università di Trento, via Mesiano, 77, I-38123 Trento, Italy
[b] School of Engineering and Material Science, Queen Mary University of London, Mile End Road, E1 4NS London, United Kingdom

ARTICLE INFO

Keywords:
Micromechanics
Time dependent Properties
Dissolvable Composites
Dissolution and Diffusion rates
Single Polymer Composites (SPCs)
Fiber Degradation

ABSTRACT

This paper proposes a novel micromechanics model tailored for dissolvable composites, where the inclusion undergoes dissolution and diffusion within the matrix, with the aim of analytically predicting the time-dependent properties of composites. The dissolution of inclusion leads to a reduction of its volume fraction and the formation of a growing interphase layer around the inclusion. This versatile model is applicable to both short-term dissolutions, as observed in the fabrication process of composites and long-term degradation occurring in high-temperature or corrosive environments, common in industrial and biological applications. Dimensionless expressions for time-dependent volume fractions of composite components are related to the dissolution and the diffusion rates, and a micromechanics three-phase model is established to evaluate the properties of the composite as a function of dissolution time. A detailed parametric study is performed to demonstrate the effect of all the parameters on the final properties. The model is successfully applied to the experimental data in the literature to show its capability and flexibility in predicting the practical dissolution examinations. The introduced model provides a pioneering framework for the future evolution of the dissolvable micromechanics concept.

1. Introduction

In the evolving landscape of modern structures and technologies, engineered materials continue to thrive, offering novel possibilities for efficient designs to address emerging challenges in material science. In the realm of modern materials, composites emerge as a paradigm, embodying the versatile integration of distinct phases, each contributing unique physical or chemical properties. These materials, characterized by the synergy of multiple components, exemplify a sophisticated approach to engineering solutions. Presently, composites find extensive applications in various domains, including civil [1,2], mechanical [3–5], aerospace [6,7], and biomedical engineering [8,9]. Composites are commonly categorized into layered, fiber-reinforced, and particle-reinforced types, with fibrous reinforcement being the predominant choice due to the inherent strength and stiffness of fibers. The use of long continuous fibers is the most effective, although chopped fiber composites are prevalent in high-volume manufacturing to mitigate costs, albeit at the expense of mechanical performance. Additionally, advancements in nanotechnology have enabled the utilization of nano-sized filler particles, offering reinforcement even in low volume fractions [10–14].

Micromechanics, a branch of continuum mechanics, predicts the effective behavior of composite materials by homogenizing constituent materials [15–19]. Simplified models, introduced by Voigt and Reuss, were later refined by Hashin and Shtrikman, while an advanced mechanics of material model considers packing geometry for realistic predictions [20–22]. Micromechanics models, rooted in elasticity theory, offer exact stress and strain distributions at the micromechanical level [23]. These models, including the self-consistent method, Mori–Tanaka method, and others, address limitations in Eshelby's solution [24–28]. Tandon and Weng combined Eshelby's and Mori–Tanaka's solutions for a closed-form solution [29], but numerical solutions are often needed for complex geometries. Semiempirical micromechanics models, like Halpin and Tsai (H-T), use curve-fitting to predict properties [29]. H-T, derived from the self-consistent micromechanics method, is widely applied, simplifying to Reuss and Voigt approximations at fitting parameters of zero and infinity [30–33].

In general, the term "phase transformation" refers to the change in the arrangement, structure, and fractions of the constituent materials, i.e., inclusions, and matrix, within the composite, leading to alterations in its overall behavior. The phases undergo transformation triggered by external stimuli and environmental factors, including temperature

* Corresponding authors.
E-mail addresses: seyedkamal.jalali@unitn.it (S.K. Jalali), nicola.pugno@unitn.it (N.M. Pugno).

https://doi.org/10.1016/j.ijmecsci.2023.108913
Received 15 September 2023; Received in revised form 28 November 2023; Accepted 8 December 2023
Available online 12 December 2023

variations, changes in applied loads, as well as exposure to aging conditions such as corrosion or degradation, leading to a range of mechanical and functional responses. Understanding and controlling phase transformations in composites are crucial for tailoring their properties to meet specific application requirements. Researchers and engineers delve into the intricate mechanisms of these transformations to optimize the performance of composites in diverse fields, including aerospace, automotive, and biomedical engineering.

Raising temperature is a key factor driving phase transformation in composites. If the temperature variation only affects individual phase properties without altering their microstructure or causing phase mixing, it's typically seen as a composite with temperature-dependent properties rather than a phase transformation. When the temperature surpasses the melting point of the phases, phase transformation becomes unavoidable, known as solid-liquid phase transformation. Phase change materials (PCM) are illustration of harnessing this type of phase transformation in composite materials, particularly in energy storage applications [34–36]. Another instance of composites with phase transformation due to component melting is found in shape memory polymers (SMPs), where semicrystalline polymer fiber network can switch between solid crystals and melt phases over the operative temperature range [37–39].

Composites reinforced with fibers made from shape memory alloys (SMA) represent another instance of phase transformation driven by temperature variation. In this case, temperature alteration doesn't induce a solid to liquid state change but rather triggers a reversible phase transformation in the microstructure of the alloy. SMA wires, often composed of nickel-titanium or copper-aluminum-nickel, undergo a phase transformation between austenite and martensite phases [40]. At higher temperatures, the alloy is in the austenitic phase, which has a higher symmetry and allows for deformation and shaping. When the alloy is cooled below a certain temperature, it transforms into the martensitic phase, characterized by a lower symmetry crystal structure. The unique aspect of SMA is their ability to revert to their original, austenitic shape when heated above a specific transition temperature. This process is reversible and can be repeated multiple times, making SMAs valuable in various engineering applications, including actuators, sensors, and medical devices [41,42].

At high enough temperatures but even lower than melting point, particularly when the chemical composition of the components is similar, elevated temperature can act as an activator for dissolution of a phase (usually a strengthener) and its diffusion within the other phase (usually the matrix) resulting in blending of phases and formation of interphase zones. An example for temperature-driven phase transformation in term of dissolution is the fabrication of single polymer composites (SPCs), where the small melting temperature difference between the fiber and the matrix poses a serious challenge [43–52], see Fig. (1*a*) from [48]. To benefit from the economic and ecological advantages of these recyclable composites, having a model for estimating the properties of the composite according to the dissolution and diffusion phenomena is vital for finding an optimal design. Reports indicate that for a high degree of dissolution, the initial reinforcing effect of inclusion expected from classical micromechanics models may be completely lost or even the properties of the composite may be weaker than that of the base matrix [53].

Unlike short-term phase transformations due to temperature variation, which typically occur in relatively short periods and occasionally during the composite production process, long-term phase transformations originating from material aging under environmental conditions gradually take place throughout the composite's lifetime. An example of gradual phase transformation due to aging is apparent in reinforced concrete with steel rebar experiencing corrosion. In this scenario, the phase transformation manifests as the ongoing diffusion of corrosion products from the steel rebar near the steel-concrete interface, as depicted in Fig. (1b). While the mass reduction of steel is restricted, the formation of a weak interphase zone leads to concrete cracking [54–56]. An additional instance of gradual phase transformation over a lifetime occurs when fiber-reinforced composites are exposed to hydraulic degradation in subsea and offshore applications. Assessments of various properties of composites subjected to aqueous media indicate a potential significant decline in mechanical properties [57–60]. A sample micrograph, as shown in Fig. (1c) from [57], displays dissolved glass

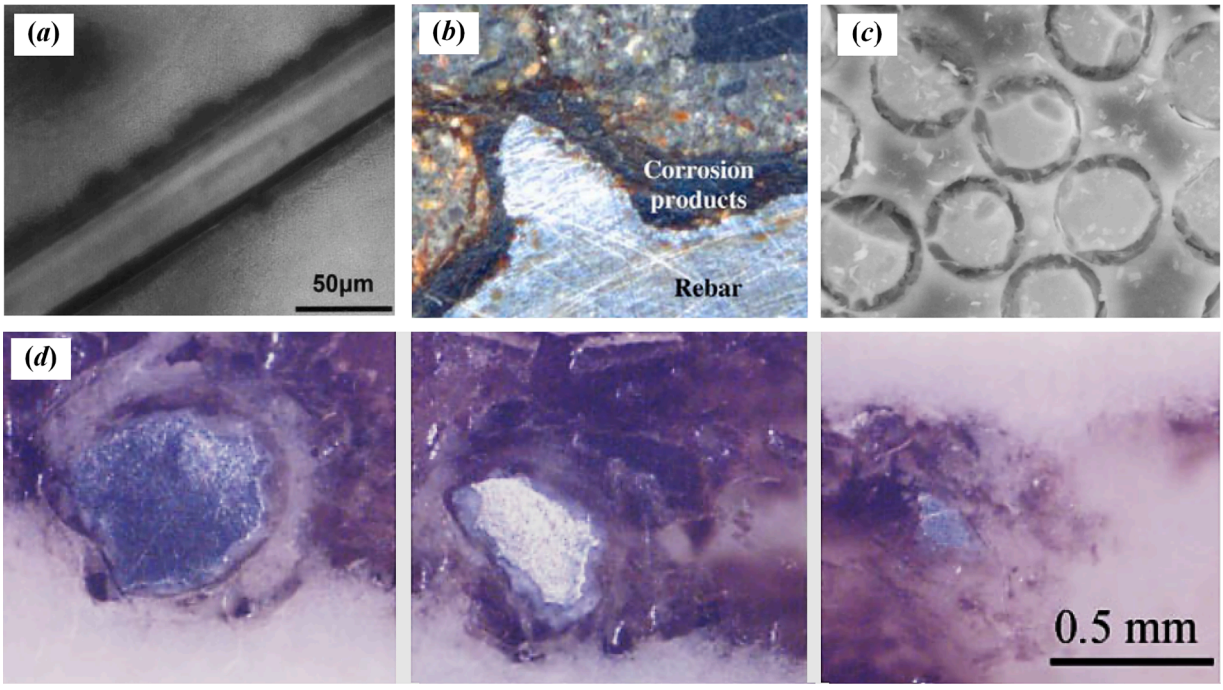

Fig. 1. Various examples of dissolvable composites. (*a*) Sample optical micrographs of a dissolved polymeric fiber in an SPC [48], (*b*) Dissolution of steel rebars in reinforced concrete due to corrosion and formation of a weak interphase zone [56], (*c*) Micrograph of dissolved glass fibers surrounded by interphase exposed to dissolution [57], (*d*) Cross-section micrographs of magnesium alloy implant after six weeks of implantation [68].

fibers surrounded by an interphase due to exposure to a solution. In contrast to the unavoidable and undesirable phase transformations in the previous two engineering applications, certain biomedical applications seek a controlled yet complete phase transformation of the reinforcement through dissolution, aiming to achieve the concept of resorbable implants [61–72]. Fig. (1d) displays cross-section micrographs of a magnesium alloy implant after six weeks of implantation, illustrating the time-lapse of the implant (inclusion) dissolution [68].

In classical micromechanics models, the assumption is typically made that the volume fraction and properties of constitutive phases remain constant over time, excluding the consideration of phase transformations. However, in the quest to understand the inherent effects of phase transformations on composite properties, several advanced models have been developed, often rooted in the foundational concepts of classical micromechanics composite models. Some have incorporated the Eshelby inclusion framework based on a mean-field micromechanical approach to elucidate phase transformations in heterogenous material systems. Romanovskaia et al. [73] utilized the generalized self-consistent field method for examining microstructural stresses in composite materials subjected to phase transformations. Incorporating the Eshelby tensor and the generalized Hooke's law, they provided a closed system of equations to determine average stresses and deformations in the phase components. As a phase transformation composite system of SMA wires embedded in an elastic matrix, Marfia and Sacco [74] studied the thermomechanical behavior of the composite, influenced by the super-elastic and shape memory effects using the Eshelby dilute distribution theory as the base of developed micromechanics model. An Eshelbian Homogenization solution for the coupled mechanical-diffusion problem of metallic matrix composite was proposed by Zhang et al. [75] and an analytical solution to the effective diffusion coefficient tensor is developed assuming it solely depended on the inclusion volume fraction. Examining the phase transformation phenomenon of interface diffusion in composites, a theoretical micromechanics framework based on Eshelby's solution was employed to analyze its significant impact on the creep behavior of metal matrix composites at high temperatures. The study considered misfit deformation and stress redistribution through the introduction of a time-evolving eigenstrain into reinforcements [76]. Pan and Weng [77] investigated thermal stress and volume changes in the phase transformation of the iron-carbon system in steel. They developed a theoretical foundation based on Eshelby's inhomogeneity and transformation principle, allowing for the consideration of factors such as elastic heterogeneity, thermal expansion coefficients, phase transformation strain, and inclusion shape.

The central focus of this study is the dissolution of reinforcing inclusions within the matrix. This process entails an ongoing decrease in the volume fraction of the inclusion, subsequently leading to the creation of an interphase zone. This zone comprises the dissolved portion of the inclusion and the involved portion of the matrix, influenced by the diffusion of the dissolved inclusion. From the standpoint of phase transformation, the composite transitions into a three-phase mixture with time-dependent volume fractions for all components. It significantly affects the properties of the composite predicted by the micromechanics models in both short-term and long-term practical scenarios. The present study aims to provide a novel update to foundational classical micromechanics models, including the rule-of-mixture (both direct and inverse) and the Halpin-Tsai equation, to enhance their applicability in predicting the properties of composites undergoing phase transformation due to dissolution. By inserting the dissolution and diffusion rates in the classical micromodel model, the volume fraction of the constituent components become variable and a function of the phase transformation time. In addition, the emergence and growth of the interphase zone, as a nested composite consists of the dissolved portion of inclusion and the portion of matrix affected by diffusion products, provides an additional degree of freedom allowing for predicting the modified properties of composite due to dissolution. Hence, despite of its inherent simplicity compared to sophisticated micromechanical models rooted in the Eshelby solution, the presented model exhibits the essential capability to analyze phase transformations in scenarios characterized by substantial changes in the volume fraction of components as observed in dissolution and degradation phenomena. This attribute can be acknowledged as an innovative feature. Notably, the model introduces a novel aspect by incorporating the dissolution dimension (one-dimensional (1D) for plate-like, two-dimensional (2D) for fiber-like, and three-dimensional (3D) for spherical-like inclusions), allowing it to account for the impact of inclusion shape on the evolution of volume fraction over dissolution time. Nevertheless, it is important to recognize that the proposed model lacks the capability to predict certain behaviors, such as the failure of the interface zone which may be manifested as a weakened bond or debonding between the inclusion and the matrix. This limitation arises from fundamental simplifications rooted in the selected classic model as the base. While these simplifications may not substantially impact the determination of elastic properties, they can influence the estimation of strength which should be acknowledged as a constraint of the current model.

The paper is structured as follows: Section 2 presents the derivation of dimensionless expressions for the volume fractions of all components, along with a detailed discussion of various scenarios for interphase growth, and inclusion and matrix fading. In Section 3, the dissolvable micromechanics model is established based on the three-phase version of classical micromechanics models, incorporating the volume fractions derived in Section 2. Finally, Section 4 applies the proposed micromechanics model to analyze experimental data from the literature. The focus is on two case studies: the fabrication of Single Polymer Composites (SPCs) addressing short-term issues and the degradation of glass fiber composites in water addressing long-term concerns.

2. Mathematical Model for Dissolution and Diffusion of Inclusions

In this section, the process of dissolution of inclusion within the composite over time is characterized and formulated and the required inputs for establishing the model in Section 3 are clearly defined and discussed. Consider an inclusion of initial volume fraction v_p^0 within a matrix of initial volume fraction of $v_m^0 = 1 - v_p^0$ and assume that the inclusion tends to be dissolved within the matrix over the time, t. At the initial state of composition, corresponding to $t = 0$, the components construct an undissolved composite obeying the 2-phase classical micromechanics models widely developed in the literature of composite materials [78,11]. Three typical geometries of inclusions i.e., plate-like, fiber-like, and sphere-like are considered and the same geometry for the surrounding matrix is assumed (see Fig. 2(a)). The initial thickness of an inclusion, D_p^0, is related to its initial volume fraction, v_p^0, as,

$$D_p^0 = \sqrt[3]{\frac{c v_p^0 V_c}{\alpha_p^{(3-n)}}}, \quad n = 1,\ 2,\ 3. \tag{1a}$$

In Eq. (1a), c is a constant related to the exact geometry of inclusion which is $6/\pi$, $4/\pi$, $4/\pi$, and 1 for spherical, cylindrical, discus, and square platelet inclusions, respectively, α_p is the aspect ratio of the inclusion (length to thickness for cylindrical, diameter to thickness for discus, and side-length to thickness for square platelet), n defines the dimension of the inclusion, which is 1, 2, and 3 for plate-like, fiber-like, and sphere-like inclusions, and V_c is the total volume of composite (see Fig. 2(a)). Regarding Eq. (1a), for an identical initial volume fraction, v_p^0, the thicknesses of fiber- and plate-like inclusions are lower than the sphere-like one due to higher aspect ratios. One can obtain the ratio of the thickness of discus and cylindrical inclusions to spherical ones as a function of aspect ratio by Eq. (1b) which is also plotted in Fig. 2(b). It reveals that for an identical initial volume fraction and aspect ratio, a plate-like inclusion has a lower thickness than the fiber-like one due to

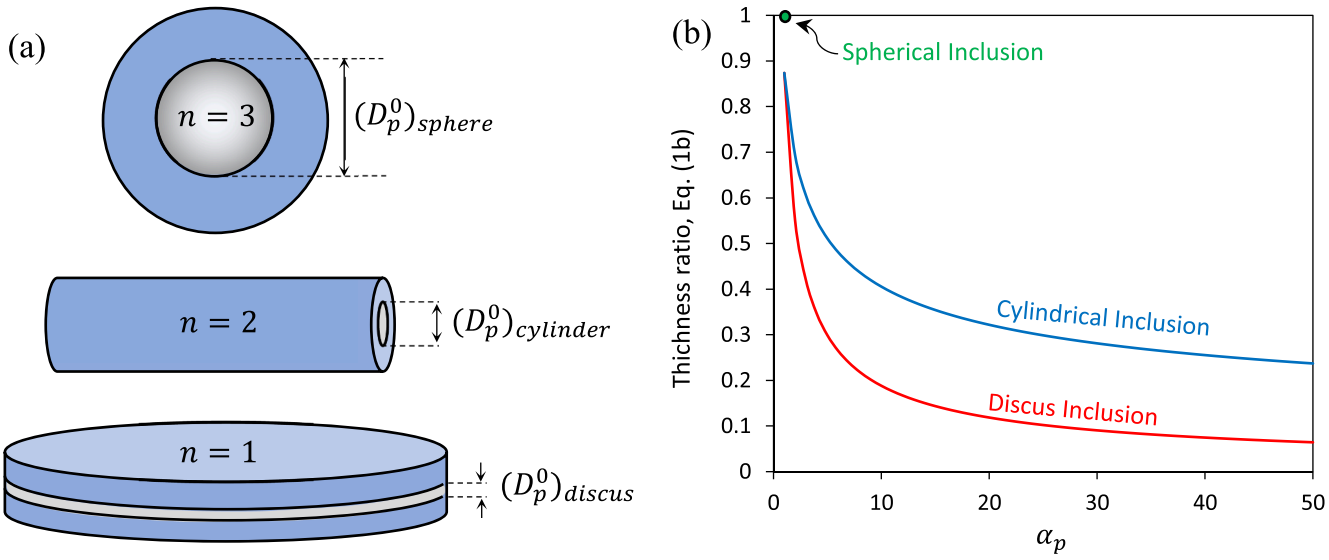

Fig. 2. The three typical geometries of inclusions. (a) Schematic of geometry of inclusions and definition of the initial inclusion thickness, D_p^0, for every configuration. (b) The effect of the aspect ratio of the plate- and fiber-like inclusions on the relative thickness with respect to sphere-like ones based on Eq. (1b). For the same initial volume fraction and aspect ratio, a plate-like inclusion shows a smaller thickness compared to a fiber-like one, attributed to its greater surface area.

its highest surface area.

$$\frac{\left(D_p^0\right)_{non-sphere}}{\left(D_p^0\right)_{sphere}} = \sqrt[3]{\frac{2}{3\alpha_p^{(3-n)}}},\ n = 1,\ 2. \tag{1b}$$

Traveling through time, the inclusion starts dissolving which results in a reduction of its volume fraction. Simultaneously, diffusion of the dissolved part of inclusion within the matrix media forms an expanding zone as an interphase between the inclusion and the matrix. Note that growth of interphase is affected by both dissolution and diffusion processes. Fig. 3(a) depicts the schematic of the formation of interphase. The dissolution rate, $q(t)$, and the diffusion rate, $p(t)$, lead the rapidity of the process. The former is mainly related to the composing process conditions (temperature and pressure) and the nature and the strength of inclusion-matrix intermolecular attractions, while the latter mainly depends on temperature (directly) and the viscosity of the matrix (inversely). It is why the dissolution and consequently diffusion phenomena are neglectable for the classical composites whose inclusion-matrix intermolecular attractions are weak and/or the matrix has quickly solidified (high viscosity).

The variation of volume, $V(t)$, with respect to time, $\dot{V}(t)$, due to dissolution and diffusion, is proportional to the front surface, $S(t)$ of dissolution and diffusion. Although, for an inclusion of general 3D shape, both dissolution and diffusion progress in 3D, however, the

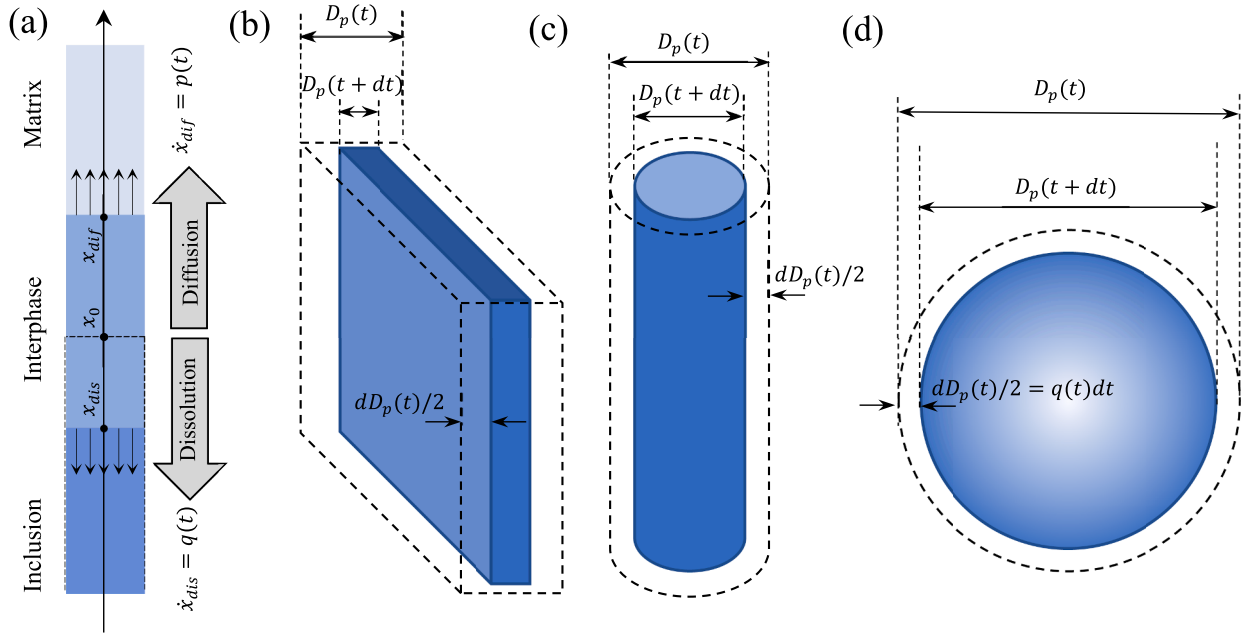

Fig. 3. Dissolution and diffusion of inclusion within the matrix and the variation of the dimension of inclusion with respect to the dissolution time. (a) Schematic of one-dimensional dissolution and diffusion of the inclusion along x-axis. Dot lines present the initial state of composition where there is no interphase and x_{dis} and x_{dif} coincide with x_0. The diffusion rate, $p(t)$, and dissolution rate, $q(t)$ lead the fronts of interphase growth which are generally time-dependent. (b) 3D dissolution, n=3, (c) 2D dissolution, n=2, (d) 1D dissolution, n=1.

geometry of inclusion determines the portion of $\dot{V}(t)$ along every spatial direction. For a sphere-like inclusion, the dissolution and diffusion progress along 3 spatial directions (3D dissolution, n=3). For a fiber-like inclusion, the ratio of ends to lateral surface is negligible, and therefore the dissolution and diffusion in the direction of the axis of inclusion can be ignored. Therefore, it can be assumed that both dissolution and diffusion happen only along the two other directions perpendicular to its axis (2D dissolution, n=2). Similarly, for a plate-like inclusion, one can neglect the in-plane directions and only consider the direction perpendicular to the plate (1D dissolution, n=1). Considering the variation of the geometry of these three types of inclusions with respect to time, schematically depicted in Fig. 3(b-d), and dissolution and diffusion rates defined in Fig. 3(a), one can formulate the variation of the thickness of the inclusion and the interphase with respect to time as,

$$\dot{D}_p(t) = -2q(t) \rightarrow D_p(t) = -2\int_0^t q(t)dt + D_p^0 \tag{2a}$$

$$\dot{D}_i(t) = 2p(t) \rightarrow D_i(t) = 2\int_0^t p(t)dt + D_p^0, \tag{2b}$$

where $D_p(t)$ represents the thickness of dissolving inclusion, $D_i(t)$ is the thickness of the interphase layer (outer dimension), and D_p^0 is the initial thickness of the inclusion (and the interphase). The dissolution and the diffusion rates are needed for obtaining the thicknesses of the inclusion and the interphase as a function of time by integrating Eqs. (2a) and (2b).

In the following it is assumed that the dissolution and the diffusion rates are constant: $q(t) = \bar{q}$, and $p(t) = \bar{p}$. Note that these average rates can generally be temperature-dependent. If their assignment is based on the corresponding temperature of the process, the predictions of the presented model will implicitly be a function of temperature. The thicknesses are obtained as,

$$D_p(t) = -2\bar{q}t + D_p^0 \tag{3a}$$

$$D_i(t) = 2\bar{p}t + D_p^0. \tag{3b}$$

The volume fractions of the inclusion, $v_p(t)$, the interphase, $v_i(t)$, and the matrix, $v_m(t)$, can be obtained as a function of time, t, as,

$$v_p(t) = v_p^0\left(\frac{D_p(t)}{D_p^0}\right)^n = v_p^0\left(\frac{-2\bar{q}t}{D_p^0}+1\right)^n, \tag{4a}$$

$$v_i(t) = v_p^0\left[\left(\frac{D_i(t)}{D_p^0}\right)^n - \left(\frac{D_p(t)}{D_p^0}\right)^n\right] = v_p^0\left[\left(\frac{2\bar{p}t}{D_p^0}+1\right)^n - \left(\frac{-2\bar{q}t}{D_p^0}+1\right)^n\right], \tag{4b}$$

$$v_m(t) = 1 - v_p^0\left(\frac{D_i(t)}{D_p^0}\right)^n = 1 - v_p^0\left(\frac{2\bar{p}t}{D_p^0}+1\right)^n. \tag{4c}$$

Some milestones should be defined on the timeline of the dissolution progress. The time when the inclusion is completely dissolved is called inclusion fading time, t_p. It can be obtained by equaling $D_p(t)$ to zero:

$$t_p = \frac{D_p^0}{2\bar{q}}. \tag{5}$$

If $t > t_p$, the volume fraction of inclusion is zero and does not obey Eq. (4a) anymore and the mixture is converted to a 2-phase composite consist of the interphase and the matrix. Diffusion of interphase is completed at the maximum diffusion time when the matrix is fully converted to the interphase which is called matrix fading time, t_m. By setting the volume fraction of matrix to zero in Eq. (4c), one obtains,

$$t_m = \frac{D_p^0}{2\bar{p}}\left(\sqrt[n]{\left(1/v_p^0\right)} - 1\right). \tag{6}$$

For $t > t_m$, there is no matrix which results in a 2-phase composite including the inclusion and the interphase. In this condition Eq. (4b) is not valid, and $D_i(t)$, remains constant as:

$$D_i(t) = D_i(t_m) = 2\bar{p}t_m + D_p^0 = D_p^0\sqrt[n]{\left(1/v_p^0\right)} = D_c, \tag{7}$$

where D_c is the dimension of the composite. Then, the volume fraction of the interphase grows only because of dissolution of the inclusion and is obtained as,

$$v_i(t) = 1 - v_p^0\left(\frac{-2\bar{q}t}{D_p^0}+1\right)^n, \text{ for } t > t_m. \tag{8}$$

Note that both the inclusion fading time, t_p, and the matrix fading time, t_m, are proportional to the initial thickness of inclusion and based on Eq. (1b), for an identical initial volume fraction of inclusion, they decrease by decreasing n and increasing the aspect ratio, α_p. The ratio of the matrix fading time, t_m, to the inclusion fading time, t_p, is,

$$\frac{t_m}{t_p} = \left(\sqrt[n]{\left(1/v_p^0\right)} - 1\right)\left(\frac{\bar{q}}{\bar{p}}\right). \tag{9}$$

By equating this ratio to one ($t_m = t_p$), the critical ratio of the dissolution to the diffusion rate can be defined as

$$t_p = t_m \rightarrow (\bar{q}/\bar{p})_{crit} = \frac{1}{\sqrt[n]{\left(1/v_p^0\right)} - 1}. \tag{10}$$

Substituting Eq. (10) in Eq. (9),

$$\frac{t_m}{t_p} = \frac{(\bar{q}/\bar{p})}{(\bar{q}/\bar{p})_{crit}}. \tag{11}$$

For this "*critical condition*", the inclusion is completely dissolved exactly when the interphase layer has just covered whole the matrix and the 3-phase composite turns suddenly to a 1-phase fully interphase material. If the dissolution to diffusion ratio, $(\bar{q}/\bar{p})$, is higher than the critical value ($t_m > t_p$), named the "*over-critical condition*", the matrix has not been fully converted to the interphase when the dissolution of the inclusion is completed, while for the $(\bar{q}/\bar{p})$ ratios lower than the critical one ($t_m < t_p$), called the "*under-critical condition*", the matrix is fully converted to the interphase before complete dissolution of the inclusion, (inclusion fading), which may result in saturation of the mixture. Fig. 4(a) depicts the variation of this critical ratio, $(\bar{q}/\bar{p})_{cri}$, versus the initial volume fraction of the inclusion, v_p^0 for 1D, 2D, and 3D dissolution. It is seen that increasing the initial volume fraction of the inclusion remarkably increases the critical ratio for all types of inclusions which means for high volume fractions of inclusions the dissolution rate should be very higher than the diffusion rate to both processes end simultaneously. In other words, for high initial fractions of the inclusion, it is more possible that the actual $(\bar{q}/\bar{p})$ ratio be under the critical one and the matrix is converted to interphase before the complete dissolution of the inclusion (under-critical condition), while low values of v_p^0 provide low critical ratio which can support the complete dissolution of the inclusion before full diffusion of the interphase in the matrix (over-critical condition). Besides, it is observed that increasing the dissolution dimension, n, increase the critical ratio for all the initial volume fractions. It means for a given value of $(\bar{q}/\bar{p})$, the plate-like inclusions have more potential for locating within the over-critical condition to completely dissolve before full diffusion of interphase while the sphere-like ones show the lowest possibility of full dissolution and may fall into the under-critical condition. This is consistent with the thickness ratio of these inclusions

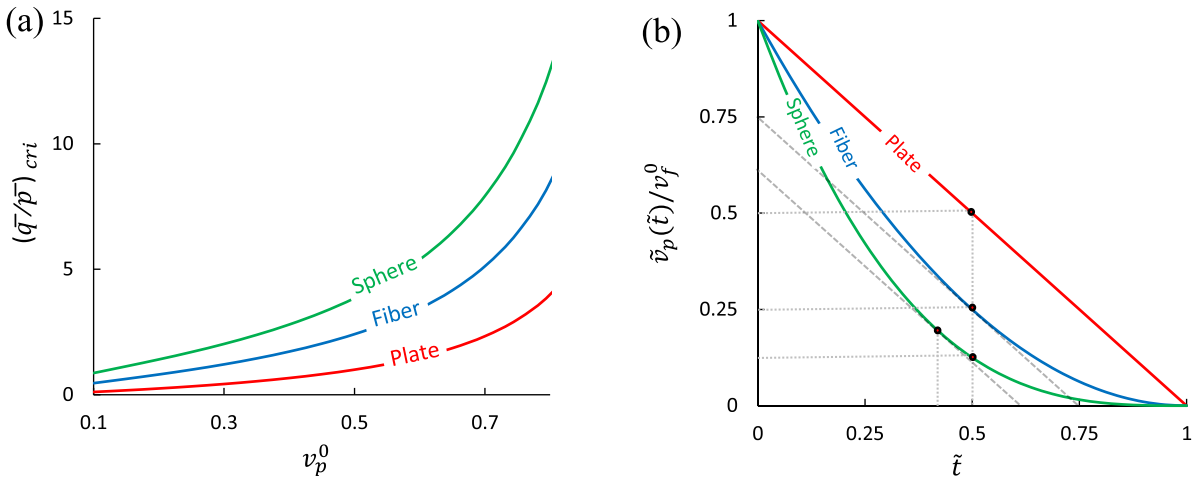

Fig. 4. Dissolution and diffusion rates and the time-dependent volume fraction of inclusion for 1D, 2D, and 3D dissolutions corresponds to plate-, fiber-, and sphere-like inclusions. (a) The variation of the critical ratio of the diffusion to the dissolution rates, $(\bar{q}/\bar{p})_{cri}$, versus the initial volume fraction of the inclusion, v_p^0. (b) The variation of dimensionless volume fraction of the inclusion versus dimensionless time within the time window from Eq. (13e).

presented in Eq. (1b) and Fig. 2(b).

The dissolution and the diffusion processes may be stopped by complete solidification of the mixture at the solidification time, $t = t_s$, which can be adjusted by controlling the environmental conditions (temperature and pressure) and/or using appropriate additives like catalyzers, initiators, and activators. If the inclusions are introduced in the matrix for playing a reinforcing role, it is desirable to stop the progress somewhen in the course of the dissolution of inclusion instead of after inclusion fading. The concept of "*dissolution window*" is defined as the time interval before completely losing the impact of inclusion on the properties of the composite. In this case, the composition process of the composite should be designed so that the solidification time, t_s, be somewhen within the dissolution window, $0 < t_s < t_p$ to optimize the demanded properties of the composite.

To generalize the formulation, the dimensionless time variables, $(\sim)$, are defined by dividing them by the fading time of inclusion, t_p, as,

$$(\tilde{t}, \tilde{t}_m, \tilde{t}_s) = (t, t_m, t_s)/t_p. \tag{12a}$$

Hence, the dimensionless dissolution window is $0 < \tilde{t} < 1$. Substituting Eq. (12a) to Eq. (11) gives,

$$\frac{(\bar{q}/\bar{p})}{(\bar{q}/\bar{p})_{crit}} = \tilde{t}_m, \tag{12b}$$

which means the condition is under-critical for $\tilde{t}_m < 1$, critical for $\tilde{t}_m = 1$, and over-critical for $\tilde{t}_m > 1$.

It should be noted that in this dimensionless timeline, there is no distinction between short-term and long-term phase transformations. If the change in composite properties in real-time is of interest, the model results need to be mapped from the dimensionless to the real-time framework using Eq. (12). The thickness of the inclusion, and the interphase, as well as the volume fraction of components, can be re-written in terms of dimensionless time by substituting Eq. (12) to Eqs. (3), (4), and (8) as,

$$D_p(\tilde{t}) = D_p^0(1-\tilde{t}), \text{ for } 0 \le \tilde{t} \le 1, \tag{13a}$$

$$D_p(\tilde{t}) = 0, \text{for } \tilde{t} > 1, \tag{13b}$$

$$D_i(\tilde{t}) = D_p^0\left(1 + \frac{\sqrt[n]{\left(1/v_p^0\right)} - 1}{\tilde{t}_m}\tilde{t}\right), \ 0 < \tilde{t} \le \tilde{t}_m, \tag{13c}$$

$$D_i(\tilde{t}) = D_p^0\sqrt[n]{\left(1/v_p^0\right)} - D_p(\tilde{t}), \text{ for } \tilde{t} > \tilde{t}_m, \tag{13d}$$

$$\tilde{v}_p(\tilde{t}) = v_p^0(1-\tilde{t})^n, \text{ for } 0 \le \tilde{t} \le 1, \tag{13e}$$

$$\tilde{v}_p(\tilde{t}) = 0, \text{ for } \tilde{t} > 1, \tag{13f}$$

$$\tilde{v}_i(\tilde{t}) = v_p^0\left(1 + \frac{\sqrt[n]{\left(1/v_p^0\right)} - 1}{\tilde{t}_m}\tilde{t}\right)^n - \tilde{v}_p(\tilde{t}), \text{ for } 0 < \tilde{t} \le \tilde{t}_m, \tag{13g}$$

$$\tilde{v}_i(\tilde{t}) = 1 - \tilde{v}_p(\tilde{t}), \text{ for } \tilde{t} > \tilde{t}_m, \tag{13h}$$

$$\tilde{v}_m(\tilde{t}) = 1 - v_p^0\left(1 + \frac{\sqrt[n]{\left(1/v_p^0\right)} - 1}{\tilde{t}_m}\tilde{t}\right)^n, \text{ for } 0 \le \tilde{t} < \tilde{t}_m, \tag{13i}$$

$$\tilde{v}_m(\tilde{t}) = 0, \text{ for } \tilde{t} > \tilde{t}_m. \tag{13j}$$

Derived from Eq. (13e) over dimensionless time, the rate of change in the volume fraction of inclusion can be found as,

$$\frac{d\left(\tilde{v}_p(\tilde{t})\right)}{d\tilde{t}} = \dot{\tilde{v}}_p(\tilde{t}) = -nv_p^0(1-\tilde{t})^{n-1}, \text{ for } 0 < \tilde{t} \le 1. \tag{14a}$$

Eq. (14a) explains that the rate of dissolution for plate-like inclusions (n=1) is constant while it reduces by the passage of $\tilde{t}$ for fiber- and sphere-like inclusions. The reason is that for plate-like inclusion the dissolution surface, $S(\tilde{t})$, does not change over time while it reduces for the other two geometries of inclusions. The rate of dissolution for the three different types of inclusion can be compared as (see Fig. 4(b)),

$$\begin{cases} \dot{\tilde{v}}_p(\tilde{t})_{fiber} > \dot{\tilde{v}}_p(\tilde{t})_{plate} & \tilde{t} < 0.5 \\ \dot{\tilde{v}}_p(\tilde{t})_{fiber} = \dot{\tilde{v}}_p(\tilde{t})_{plate} & \tilde{t} = 0.5 \\ \dot{\tilde{v}}_p(\tilde{t})_{fiber} < \dot{\tilde{v}}_p(\tilde{t})_{plate} & \tilde{t} > 0.5, \end{cases} \tag{14b}$$

$$\begin{cases} \dot{\tilde{v}}_p(\tilde{t})_{sphere} > \dot{\tilde{v}}_p(\tilde{t})_{plate} & \tilde{t} < \left(1 - 1/\sqrt{3}\right) \cong 0.42 \\ \dot{\tilde{v}}_p(\tilde{t})_{sphere} = \dot{\tilde{v}}_p(\tilde{t})_{plate} & \tilde{t} = \left(1 - 1/\sqrt{3}\right) \cong 0.42 \\ \dot{\tilde{v}}_p(\tilde{t})_{sphere} < \dot{\tilde{v}}_p(\tilde{t})_{plate} & \tilde{t} > \left(1 - 1/\sqrt{3}\right) \cong 0.42. \end{cases} \tag{14c}$$

The variation of dimensionless volume fraction of the inclusion versus dimensionless time within the time window is depicted in Fig. 4

(b) for 1D, 2D, and 3D dissolutions based on Eq. (13e). It is seen that at every dimensionless time, $\tilde{t}$, by increasing the dissolution dimension, n, the percentage of reduction in the initial volume fraction of inclusion increases. For instance, at the middle of the time window, $\tilde{t} = 0.5$, the percentage of reduction in the volume fraction of sphere-, fiber-, and plate-like inclusions are 87.5%, 75%, and 50%, respectively. Note that the time scale in Fig. 4(b) is dimensionless and the mentioned comparison for the effect of n is not valuable for the real time, t, since according to Eqs. (1b), (5), and (6), for an identical initial volume fraction, different types of inclusions have different inclusion fading times, t_p. Besides, the rate of changes in volume fraction presented by Eq. (14 a-c) can be observed as the slopes of the graphs. The slope for 1D dissolution corresponding to plate-like inclusions is constant as the dissolution process does not change the facing surface and only reduces the thickness. For 2D and 3D cases, the surface area reduces over time which results in a reduction in the dissolution rate.

Fig. 5(a-c) demonstrates how the interphase grows for under-critical, critical, and over-critical conditions, respectively. Two different low ($v_p^0 = 0.1$), and high ($v_p^0 = 0.8$) initial volume fractions of the inclusion are considered and the effect of different dissolution dimensions, n, is investigated. In Fig. 5(a) the dimensionless matrix fading time, $\tilde{t}_m$, is assumed equal to 0.25 which means $(\bar{q}/\bar{p})$ is a quarter of its critical value, to present a case of under-critical condition. In the first part ($0 < \tilde{t} < 0.25$), the formation of interphase is due to both dissolution and diffusion processes constructing a 3-phase composite. However, at $\tilde{t} = 0.25$ interphase reaches the outer boundary of the composite (matrix fading happens). In the second part of the graph, from matrix fading to the end of the time window ($0.25 < \tilde{t} < 1$), the diffusion is stopped, and the growth of interphase is solely due to dissolution of inclusion, and it is why increasing the dissolution dimensions, n, results in higher volume fraction of interphase regarding the trend observed in Fig. 4(b). Finally, at $\tilde{t} = 1$ the inclusion also completely turns to interphase, and interphase cover whole the composite. Fig. 5(b) shows the critical condition where

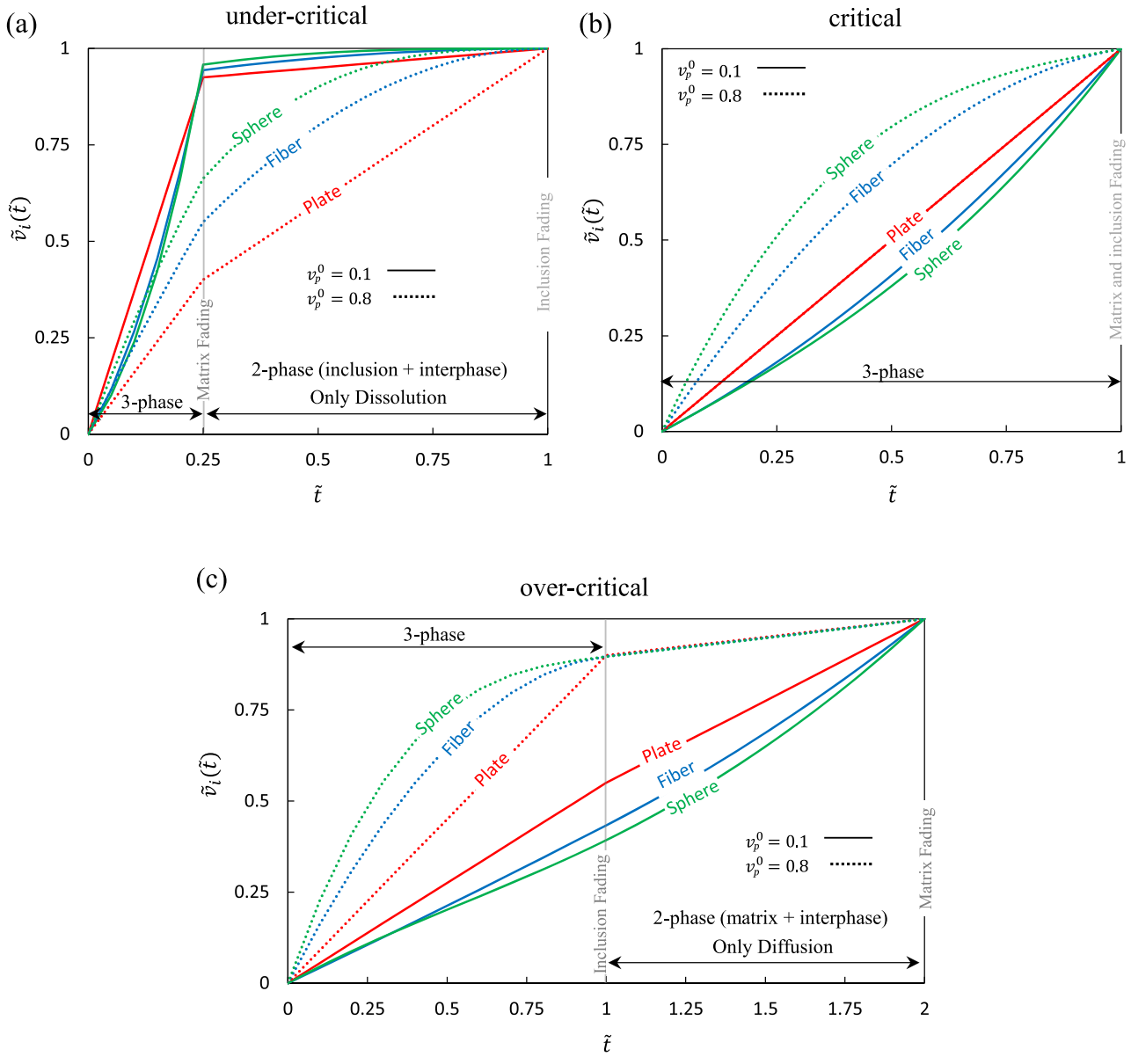

Fig. 5. The variation of dimensionless volume fraction of interphase with respect to dimensionless time. (a) under-critical condition where the matrix fading happens before the inclusion fading as a result of ratio of dissolution to diffusion rate lower than the critical ratio. (b) critical condition where the inclusion and matrix fading happens simultaneously. and (c) over-critical condition where the inclusion fading happens before the matrix fading because of ratio of dissolution to diffusion rate higher than the critical ratio. See Eqs. (9) to (11).

$\widetilde{t}_m = 1$ and the fading of the inclusion and the matrix happens simultaneously at the end of the time window, $\widetilde{t} = 1$. Throughout whole the time window, all three phases exist, and the growth of interphase is led by both diffusion and dissolution fronts. It is seen that for $v_p^0 = 0.1$ increasing n reduces the dimensionless volume fraction of interphase while for $v_p^0 = 0.8$ it is the opposite. The reason is that for low initial volume fractions of inclusion the main part of interphase growth is due to the diffusion but for high initial fractions the most part of the development of interphase corresponds to the dissolution of inclusions which is higher when n increases based on the trend observed in Fig. 4 (b). An example of an over-critical condition is presented in Fig. 5(c) by setting the dimensionless matrix fading time as $\widetilde{t}_m = 2$. Since $\widetilde{t}_m > 1$, the mixing process continues after closing the time window (inclusion fading) by diffusion of interphase until the interphase covers whole the composite ($\widetilde{t} = 2$). The effect of the dissolution dimension, n, on the volume fraction of interphase is the same as the critical condition explained in Fig. 5(b). One can notice that increasing the initial volume fraction increases the volume fraction of interphase since the inclusion is fully converted to the interphase at the end of the time window ($\widetilde{t} = 2$).

The composition ends when both the inclusion and the matrix are faded and whole the mixture turns to the interphase and the composite converts to a 1-phase material at $\widetilde{t} = \widetilde{t}_e$. From Fig. 5 it is seen that this ending time is,

$$\widetilde{t}_e = \begin{cases} 1 & \text{Under} - \text{Critical} \\ 1 & \text{Critical} \\ \widetilde{t}_m & \text{Over} - \text{Critical.} \end{cases} \tag{15}$$

It is concluded that for formulating the dissolution and diffusion processes it is essential to know the fading time of the inclusion, t_p, and the matrix, t_m. Given the inclusion fading time, $\widehat{t}_p$, and the matrix fading time, $\widehat{t}_m$, for a specific initial volume fraction of the inclusion, $\widehat{v}_p^0$, and initial thickness, $\widehat{D}_p^0$, measured experimentally or estimated through molecular simulations, it is possible to find the dissolution and diffusion rates and their ratio using Eqs. (5), (6), and (9) which are constant for all the initial volume fractions and thicknesses of the same matrix and inclusion as,

$$\bar{q} = \frac{\widehat{D}_p^0}{2\widehat{t}_p}, \tag{16a}$$

$$\bar{p} = \frac{\widehat{D}_p^0}{2\widehat{t}_m} \sqrt[n]{\left(1 \middle/ \widehat{v}_p^0\right)} - 1, \tag{16b}$$

$$\frac{\bar{q}}{\bar{p}} = \frac{\left(\widehat{t}_m \middle/ \widehat{t}_p\right)}{\sqrt[n]{\left(1 \middle/ \widehat{v}_p^0\right)} - 1}. \tag{16c}$$

Having the ratio of dissolution to diffusion rate by Eq. (16c) and calculating the critical ratio using Eq. (10), the condition (under-critical, critical, and over-critical) is determined for every initial volume fraction of inclusion (see Fig. 4(a)). Then, from Eqs. (5) and (6) one can obtain the inclusion and the matrix fading time corresponds to an arbitrary initial volume fraction v_p^0 and initial thickness of D_p^0 as,

$$t_p = \widehat{t}_p \left(D_p^0 \middle/ \widehat{D}_p^0\right), \tag{17a}$$

$$t_m = \widehat{t}_m \left(D_p^0 \middle/ \widehat{D}_p^0\right) \frac{\sqrt[n]{\left(1 \middle/ v_p^0\right)} - 1}{\sqrt[n]{\left(1 \middle/ \widehat{v}_p^0\right)} - 1}. \tag{17b}$$

As the final part of this section, the composition of the interphase is under focus. The interphase consists of the dissolute part of the inclusion and the part of the matrix engaged by the diffusion. Hence, the dimensionless volume fraction of interphase, $\widetilde{v}_i(\widetilde{t})$, can be divided into these two parts as,

$$\widetilde{v}_{ip}(\widetilde{t}) = v_p^0 - \widetilde{v}_p(\widetilde{t}), \tag{18a}$$

$$\widetilde{v}_{im}(\widetilde{t}) = \widetilde{v}_i - \widetilde{v}_{ip}(\widetilde{t}), \tag{18b}$$

where $\widetilde{v}_{ip}(\widetilde{t})$, and $\widetilde{v}_{im}(\widetilde{t})$ are the parts that corresponds to the dissolution of the inclusion and the diffusion in the matrix, respectively. It is useful to define the partial volume fraction of the inclusion, $\widetilde{f}_{ip}(\widetilde{t})$, and the matrix, $\widetilde{f}_{im}(\widetilde{t})$, within the interphase as,

$$\widetilde{f}_{ip}(\widetilde{t}) = \widetilde{v}_{ip}(\widetilde{t}) \big/ \widetilde{v}_i(\widetilde{t}),\ \widetilde{t} > 0, \tag{18c}$$

$$\widetilde{f}_{im}(\widetilde{t}) + \widetilde{f}_{ip}(\widetilde{t}) = 1 \rightarrow \widetilde{f}_{im}(\widetilde{t}) = 1 - \widetilde{f}_{ip}(\widetilde{t}),\ \widetilde{t} > 0. \tag{18d}$$

3. Establishing the Micromechanics Model for Dissolvable Composites

In this section, the focus turns to the construction of a micromechanics model tailored for dissolvable composites. The steps of the proposed analytical framework are navigated, commencing with a definition of the required inputs. Moving forward, the properties of the interphase are estimated based on the properties of both the matrix and the inclusion from which the interphase originates. Subsequently, the estimation of the elastic constants of the dissolvable composites will then be expounded upon. Lastly, the examination of strength is discussed. It is crucial to acknowledge that the presented model lacks the capability to predict specific behaviors, such as potential failures in the interface zone, characterized by a weakened bond or debonding between the inclusion and the matrix. This limitation arises from fundamental simplifications rooted in the selected classical model as its basis. While these simplifications may not markedly influence the determination of elastic properties, they can affect strength estimation. However, it is essential to distinguish between the phase transformation in the form of dissolution, which typically occurs due to an increase in temperature, and gradual degradation, which results from an unfavorable environment, such as corrosion. In the former, dissolution may even lead to improved bonding between the inclusion and the matrix, whereas in the latter, the effect is often the opposite.

3.1. Inputs of the Proposed Model

All micromechanics models are constructed based on the properties of components and the parameters determining how they are combined. Unlike classical (undissolvable and time-independent) micromechanics models, the proposed time-dependent dissolvable model also needs the parameters that formulate the dissolution and diffusion processes. The required inputs of the model are:

- The initial volume fraction, v_p^0, and the initial thickness, D_p^0, of the inclusion.
- The geometrical parameters (aspect ratio) and the dispersion condition of inclusion within the matrix.
- The fading time of the inclusion, $\widehat{t}_p$, the fading time of the matrix, $\widehat{t}_m$, and the properties in the final 1-phase condition (fully interphase) at ending time for a typical sample with initial values of $\widehat{v}_p^0$ and $\widehat{D}_p^0$.
- The properties of the inclusion: It is assumed that the undissolved part of the inclusion keeps its initial properties during the composition process. Hence, the properties of the inclusion are time-independent: $P_p(\widetilde{t}) = P_p(0) = P_p^0$. However, for more compliance with the reality, it is suggested to measure the properties of the

inclusion after applying the condition of the composition (for composition in high temperature the properties of annealed inclusion).

- The properties of the matrix: As the matrix may contain the additives (catalyzers, initiators, activators, etc.) to control the solidification time, t_s, its properties are generally time-dependent. It is suggested to measure the properties of the matrix at different times to approximate its properties as a function of composition time: $P_m(\tilde{t})$. A linear approximation can be assumed as,

$$P_m(\tilde{t}) = \beta_P \tilde{t} + P_m^0. \tag{19a}$$

Given the properties of the matrix, P_m^0 at the begging, $\tilde{t} = 0$, and P_m^e at the ending time, $\tilde{t} = \tilde{t}_e$, the slope, β_P, can be calculated as follows,

$$\beta_P = \frac{P_m^e - P_m^0}{\tilde{t}_e}. \tag{19b}$$

As a conclusive point, it is crucial to recognize that the initial properties of the components and their alterations during the dissolution process may be temperature-dependent. Hence, if the temperature-dependent behavior or changes in these properties are known, the model can effectively account for the temperature's impact on predicting the transformed properties of the composite.

3.2. Properties of the Interphase

To completely define the inputs of the model, the properties of the interphase, $P_i(\tilde{t})$, should be estimated based on the properties of the matrix and the inclusion from which it is formed. Three different formulations including direct rule-of-mixture (the Voigt model), inverse rule-of-mixture (the Reuss model), and the Halpin-Tsai semiempirical equation (H-T model) can be employed as,

$$P_i(\tilde{t}) = \tilde{f}_{ip}(\tilde{t})\left(P_p^0\right)_{eff} + \tilde{f}_{im}(\tilde{t})(P_m(\tilde{t}))_{eff}, \ \text{(Voigt Model)}, \tag{20a}$$

$$P_i(\tilde{t}) = \frac{\left(P_p^0\right)_{eff}(P_m(\tilde{t}))_{eff}}{\tilde{f}_{im}(\tilde{t})\left(P_p^0\right)_{eff} + \tilde{f}_{ip}(\tilde{t})(P_m(\tilde{t}))_{eff}}, \ \text{(Reuss Model)}, \tag{20b}$$

$$P_i(\tilde{t}) = (P_m(\tilde{t}))_{eff}\frac{1 + \xi\eta^i(\tilde{t})\tilde{f}_{ip}(\tilde{t})}{1 - \eta^i(\tilde{t})\tilde{f}_{ip}(\tilde{t})}, \ \text{(H}-\text{T model)}, \tag{20c}$$

$$\eta^i(\tilde{t}) = \frac{\left(\left(P_p^0\right)_{eff} \Big/ (P_m(\tilde{t}))_{eff}\right) - 1}{\left(\left(P_p^0\right)_{eff} \Big/ (P_m(\tilde{t}))_{eff}\right) + \xi}, \tag{20d}$$

where ξ is the curve-fitting parameter of the H-T model, and the partial volume fractions, $\tilde{f}_{ip}(\tilde{t})$, and $\tilde{f}_{im}(\tilde{t})$ are defined in Eqs. (18c) and (18d). The "*effective property*" of the inclusion and the matrix within the interphase are defined by introducing the concept of efficiency parameter to account for the influence of mixing condition (effect of additives, chemical, and physical modifications) on their original properties outside the interphase zone as,

$$\left(P_p^0\right)_{eff} = (1 + \gamma_P)P_p^0, \ \text{(The effective property of inclusion)}, \tag{21a}$$

$$(P_m(\tilde{t}))_{eff} = \left(1 + \gamma_P'\right)P_m(\tilde{t}), \ \text{(The effective property of matrix)}. \tag{21b}$$

The case of $\gamma_P = \gamma_P' = 0$, turns Eqs. (20 a-d) to their standard form meaning that the properties of the inclusion and the matrix do not change in the interphase, while negative and positive efficiencies support diminishing and enhancing effects, respectively. In general, the efficiency parameter of the inclusion is time-dependent, however, it is possible to estimate it by evaluating Eq. (20) for the property of 1-phase composite (fully interphase) measured at the ending time for a specific initial volume fraction of the inclusion, $\hat{v}_p^0$ to have an insight about an average value for the efficiency parameters. Note that the choice among Eqs. (20 a-c) should be consistent with the dissolvable micromechanics model used for predicting the properties of the composite which is introduced in the following subsections.

3.3. Elastic Constants of the Dissolvable Composites

Reviewing the literature of the micromechanics model, three main formulations for prediction of the elastic constants of composites including elastic modulus, shear modulus, and Poisson's ratio are the Voigt, (direct rule-of-mixture), the Reuss (inverse rule-of-mixture), and the semi-empirical Halpin-Tsai models, as used in the previous section for the properties of the interphase. Here, their 3-phase versions are developed based on the assumptions of the proposed dissolvable micromechanics model where time-dependent volume fractions of the components are defined in Eqs. (13) and (18).

3.3.1. The 3-phase Voigt model for dissolvable composites

The properties of the dissolvable composite as a function of dimensionless time, $P_c(\tilde{t})$, can be predicted via a 3-phase direct rule-of-mixture as,

$$P_c(\tilde{t}) = P_p^0\tilde{v}_p(\tilde{t}) + P_m(\tilde{t})\tilde{v}_m(\tilde{t}) + P_i(\tilde{t})\tilde{v}_i(\tilde{t}). \tag{22a}$$

By substituting the properties of the matrix and the interphase from Eqs. (19), and (20a) and some simplifications:

$$\begin{aligned} P_c(\tilde{t}) = {} & P_p^0\left(v_p^0(1 + \gamma_P) - \gamma_P\tilde{v}_p(\tilde{t})\right) \\ & + \left(\beta_P\tilde{t} + P_m^0\right)\left(\left(1 - v_p^0\right) + \gamma_P'\left(\tilde{v}_p(\tilde{t}) + \tilde{v}_i(\tilde{t}) - v_p^0\right)\right). \end{aligned} \tag{22b}$$

It is seen that for the case of $\gamma_P = \gamma_P' = 0$, and constant properties of the matrix, $\beta_P = 0$, Eq. (22b) turns to the standard 2-phase time-independent rule-of-mixture because $\gamma_P = \gamma_P' = 0$ means that the engaged parts of the inclusion, and the matrix within the interphase, keep their properties and it is not the matter where these parts exist in the composite. In other words, for this special case, the dissolution and diffusion processes do not affect the properties of the composite. If the property of matrix within the interphase remains unchanged, $\gamma_P' = 0$, and only the property of the dissolved part of the inclusion be modified in the interphase, Eq. (22b) is rewritten as,

$$P_c(\tilde{t}) = P_p^0\left(v_p^0(1 + \gamma_P) - \gamma_P\tilde{v}_p(\tilde{t})\right) + \left(\beta_P\tilde{t} + P_m^0\right)\left(1 - v_p^0\right). \tag{22c}$$

3.3.2. The 3-phase Reuss model for dissolvable composites

The 3-phase version of inverse rule-of-mixture known as the Reuss model is employed to develop the time-dependent dissolvable micromechanics model for predicting the properties of composite as,

$$P_c(\tilde{t}) = \frac{P_p^0 P_m(\tilde{t})P_i(\tilde{t})}{\tilde{v}_p(\tilde{t})P_m(\tilde{t})P_i(\tilde{t}) + \tilde{v}_m(\tilde{t})P_p^0P_i(\tilde{t}) + \tilde{v}_i(\tilde{t})P_p^0P_m(\tilde{t})}. \tag{23a}$$

Replacing the properties of the matrix and the interphase by Eqs. (19), and (20b), one can rewrite Eq. (23a) as,

$$P_c(\tilde{t}) = \frac{P_p^0(1+\gamma_P)\left(1+\gamma_P^{'}\right)\left(\beta_P\tilde{t}+P_m^0\right)}{P_p^0(1+\gamma_P)\left((1+\gamma_P^{'})\tilde{v}_m(\tilde{t})+\tilde{v}_p(\tilde{t})+\tilde{v}_i(\tilde{t})-v_p^0\right)+\left(\beta_P\tilde{t}+P_m^0\right)(1+\gamma_P^{'})\left((1+\gamma_P)\tilde{v}_p(\tilde{t})+v_p^0-\tilde{v}_p(\tilde{t})\right)}. \tag{23b}$$

Note that for the case of $\gamma_P = \gamma_P^{'} = \beta_P = 0$, Eq. (23b) is simplified to standard undissolvable, time-independent form. If $\gamma_P \neq 0$, while $\gamma_P^{'} = 0$, Eq. (23b) is more simplified as:

$$P_c(\tilde{t}) = \frac{P_p^0(1+\gamma_P)\left(\beta_P\tilde{t}+P_m^0\right)}{P_p^0(1+\gamma_P)\left(1-v_p^0\right)+\left(\beta_P\tilde{t}+P_m^0\right)\left(v_p^0+\gamma_P\tilde{v}_p(\tilde{t})\right)}. \tag{23c}$$

3.3.3. The 3-phase Halpin-Tsai (H-T) equation for dissolvable composites

The construction of the 3-phase model based on the original 2-phase H-T equation needs to look at the dissolvable composite as a 2-step nested mixture: The first step is the composition of the inclusion with the interphase, and the second step is the composition of the composite of the first step with the matrix. The time-dependent properties of the inclusion-interphase mixture, $P_c^{ip}(\tilde{t})$, is obtained as,

$$P_c^{i+p}(\tilde{t}) = P_i(\tilde{t})\frac{1+\xi\eta^{i+p}(\tilde{t})\tilde{v}_{i+p}(\tilde{t})}{1-\eta^{i+p}(\tilde{t})\tilde{v}_{i+p}(\tilde{t})}, \tag{24a}$$

where

$$\eta^{i+p}(\tilde{t}) = \frac{\left(P_p^0/P_i(\tilde{t})\right)-1}{\left(P_p^0/P_i(\tilde{t})\right)+\xi}, \tag{24b}$$

$$\tilde{v}_{i+p}(\tilde{t}) = \frac{\tilde{v}_p(\tilde{t})}{\tilde{v}_p(\tilde{t})+\tilde{v}_i(\tilde{t})}. \tag{24c}$$

The final properties of composites, $P_c(\tilde{t})$, is obtained by a combination of the properties of the first step, $P_c^{i+p}(\tilde{t})$, and the properties of the matrix as,

$$P_c(\tilde{t}) = P_m(\tilde{t})\frac{1+\xi\eta^{i+p+m}(\tilde{t})\tilde{v}_{i+p+m}(\tilde{t})}{1-\eta^{i+p+m}(\tilde{t})\tilde{v}_{i+p+m}(\tilde{t})}, \tag{24d}$$

where

$$\eta^{i+p+m}(\tilde{t}) = \frac{\left(P_c^{i+p}(\tilde{t})/P_m(\tilde{t})\right)-1}{\left(P_c^{i+p}(\tilde{t})/P_m(\tilde{t})\right)+\xi}, \tag{24e}$$

$$\tilde{v}_{i+p+m}(\tilde{t}) = \tilde{v}_p(\tilde{t})+\tilde{v}_i(\tilde{t}). \tag{24f}$$

In Eqs. (24), ξ is the curve-fitting parameter of the H-T model, and the properties of the matrix and the interphase are obtained from Eqs. (19), and (20 c-d), respectively.

3.3.4. The parametric study of the elastic constants

In this subsection, a comprehensive parametric study on the elastic properties of dissolvable composites is performed based on the three developed models. Regarding the literature of composite materials, two main categories of composites correspond to continuous (long) and discontinuous (short) inclusions. For the continuous composites the length of inclusion is long enough (much larger enough than a critical length), and the inclusion is able to carry the part of applied stress corresponds to its volume fraction, while for the discontinuous one interfacial shear strength between the components has the main rule for the load transformation between adjacent components. For the introduced plate- and fiber-like inclusion both continuous and discontinuous conditions are reachable by adjusting the aspect ratio, however, adding the sphere-like inclusion in a matrix only results in a discontinuous composite. Table 1 summarizes which model is the best choice for the prediction of the elastic property of continuous and discontinuous composites according to the literature of the micromechanics of composites. For aligned inclusions (plate- and fiber-likes), the longitudinal direction refers to the direction of the larger dimension of the inclusions and the transverse direction is perpendicular to it. Note that for the case of randomly oriented inclusions, the elastic constants can be calculated by averaging the elastic constants of aligned ones over all possible orientations by integration [79,80].

In the following, first, the parametric study is performed based on the 3-phase Voigt model proposed in Eq. (22) and then this model is compared to the Reuss and the H-T models. Besides, note that the time-dependent properties of the dissolvable composite arise from two sources: changes in the properties of the engaging parts of the inclusion, and the matrix within the interphase, and the time-dependent properties of the matrix which are represented in the proposed models by introducing γ_P, $\gamma_P^{'}$, and β_P parameters, respectively. The presented parametric study assumes that the properties of the matrix inside and outside the interphase zone is the same, $\gamma_P^{'} = 0$, to limit the degree of freedom. Derived from Eq. (22c) over dimensionless time for the Voigt model, and substituting from Eq. (14a), the rate of change in the properties of the composite can be found as,

$$\frac{d(P_c(\tilde{t}))}{d\tilde{t}} = \gamma_P\left(nP_p^0v_p^0\right)(1-\tilde{t})^{n-1}+\beta_P\left(1-v_p^0\right), 0<\tilde{t}<1(\text{All conditions}), \tag{25a}$$

$$\frac{d(P_c(\tilde{t}))}{d\tilde{t}} = \beta_P\left(1-v_p^0\right), 1<\tilde{t}<\tilde{t}_m(\text{Only over}-\text{critical}). \tag{25b}$$

Remember from Eq. (15) that the ending time for under-critical, and critical conditions is $\tilde{t}_e = 1$ while for the over-critical condition is $\tilde{t}_e = \tilde{t}_m$. From Eq. (25a) it is seen that within the time window, $0<\tilde{t}<1$, both γ_P, and β_P parameters are engaged. If they have the same sign, the properties of the composite are strictly ascending or strictly descending for positive and negative signs, respectively, while different signs of γ_P, and β_P may result in an extremum when,

$$\frac{d(P_c(\tilde{t}))}{d\tilde{t}} = 0 \rightarrow \tilde{t}_{ext} = 1-\left(-\frac{\beta_P\left(1-v_p^0\right)}{\gamma_P\left(nP_p^0v_p^0\right)}\right)^{n-1}. \tag{25c}$$

This extremum exists if $\tilde{t}_{ext}<1$. Over the time window, $1<\tilde{t}<\tilde{t}_m$, which only happens for over-critical conditions, only β_P can play a role

Table 1
The suggested micromechanics models based on the literature of composites [78,11].

	Inclusion Types	Property	Model
Continuous	Plate-like	Longitudinal Modulus, E_L	Voigt
	Fiber-like	In-plane Poisson's ratio, ν	Voigt
		Transverse Modulus, E_T	*Reuss, H-T
		In-Plane Shear Modulus, G	*Reuss, H-T
Discontinuous	Plate-like	Longitudinal Modulus, E_L	H-T
	Fiber-like	In-plane Poisson's ratio, ν	Voigt
	Sphere-like	Transverse Modulus, E_T	H-T
		In-Plane Shear Modulus, G	H-T

* The Reuss model is not accurate enough.

since the dissolution process of the inclusion has finished at $\tilde{t} = 1$. For the special case where the properties of the matrix are time-independent, $P_m(\tilde{t}) = P_m^0$, corresponds to $\beta_P = 0$, as the term $(nP_p^0 v_p^0)$ in Eq. (25a) is always positive, the variation of $P_c(\tilde{t})$ with respect to $\tilde{t}$ has the same sign of γ_P, and for the plate-like inclusions, $n = 1$, it is constant while for the fiber- and sphere-like inclusions, $n = 2$, and 3, it decreases gradually to zero at $\tilde{t} = 1$. According to Eq. (25b), the properties of composite remain constant for the over-critical conditions since $\beta_P = 0$.

To increase the clarity of parametric study, in the following, first, the properties of the matrix are assumed time-independent, $\beta_P = 0$, to focus on the effect of γ_P, and then the combined effect is investigated. Besides, the following dimensionless ratios of properties are defined as,

$$R_{pm}^0 = \frac{P_p^0}{P_m^0}, \text{The ratio of the initial properties of the inclusion to the matrix,} \tag{26a}$$

$$R_{cm}(\tilde{t}) = \frac{P_c(\tilde{t})}{P_m^0}, \text{The reinforcing parameter of the composite,} \tag{26b}$$

$$\bar{R}_{cm}(\tilde{t}) = \frac{R_{cm}(\tilde{t})}{R_{cm}(0)}, \text{The normalized reinforcing parameter of the composite.} \tag{26c}$$

The normalized dimensionless reinforcing parameter, $\bar{R}_{cm}(\tilde{t})$, is obtained by dividing the reinforcing parameter, $R_{cm}(\tilde{t})$, by its initial value at $\tilde{t} = 0$. Hence, its variation with respect to $\tilde{t}$ represents the effect of dissolution and diffusion processes compared to its undissolvable, time-independent counterpart. The percent of changes in this normalized parameter at the end of the time window, $\tilde{t} = 1$, is defined as,

$$\Delta\bar{R}_{cm}(\%) = \frac{\bar{R}_{cm}(1) - \bar{R}_{cm}(0)}{\bar{R}_{cm}(0)} \times 100 = (\bar{R}_{cm}(1) - 1) \times 100. \tag{26d}$$

Fig. 6(a) shows the variation of normalized dimensionless reinforcing parameter, $\bar{R}_{cm}(\tilde{t})$, through the normalized time window, $0 \le \tilde{t} \le 1$ for different types of inclusions, n=1, 2, and 3. It is assumed that the properties of the matrix are time-independent, $P_m(\tilde{t}) = P_m^0$, $(\beta_P = 0)$, and the effect of the efficiency parameter of the inclusion in the interphase, γ_P, is investigated. It is seen that for $\gamma_P = 0$ the properties of the composite are time-independent as dissolution of the inclusion does not change its properties and its total amount in the composite. However, positive, and negative values of γ_P increases and decreases the properties of composite with respect to $\tilde{t}$, respectively (see Eq. (25a)). It is seen that the 3D dissolution, $n = 3$, experiences the highest variation and the 1D shows the lowest, nevertheless, for a specific value of γ_P, all types of inclusions result in the same properties of a composite at the end of the time window, $\tilde{t} = 1$, when the inclusions completely fade, and it will be constant for $\tilde{t} > 1$ for the over-critical conditions as the properties of the matrix is assumed time-independent (diffusion of interphase through the matrix does not change the properties and the total amount of the matrix within the composite, see Eq. (25b)). Since $\beta = 0$, according to Eq. (25c), the extremum happens at $\tilde{t} = 1$. As the effect of negative and positive values of γ_P are symmetric with respect to $\bar{R}_{cm}(\tilde{t}) = 1$, in the upcoming parametric studies, only its negative values are chosen.

Fig. 6 (b) and (c) respectively prob the influence of the initial volume fraction of the inclusion, v_p^0, and the relative properties of the inclusion to the matrix, R_{pm}^0, on the percent of changes in the normalized parameter, $\Delta\bar{R}_{cm}$, assuming constant properties for the matrix, $\beta_P = 0$. Note that $\Delta\bar{R}_{cm}$ is not affected by dissolution dimension, n, as $\bar{R}_{cm}(1)$ is the same for all types of the inclusions (see Fig. 6(a)). From Fig. 6(b) one can observe that increasing γ_P linearly increases the changes in the properties of composite with respect to time and for all values of γ_P increasing the initial volume fraction of the inclusion, v_p^0, causes higher changes in the properties of the composite, $\Delta\bar{R}_{cm}$, because the only reason for time-dependent properties is the changes in the properties of the dissolved inclusion (the higher v_p^0, the higher changes). In Fig. 6(a-b) the properties of the inclusion are considered 10 times of the matrix, $R_{pm}^0 = 10$. The effect of this parameter, on $\Delta\bar{R}_{cm}$ is investigated in Fig. 6 (c) for different initial volume fractions of the inclusion. A high value of $\gamma_P = 0.9$ corresponds to a 90% reduction in the properties of the inclusion due to dissolution is chosen to represent a case with high time-dependency. It is seen that increasing R_{pm}^0 from 10 to a high value of 100 increases the changes in the properties of the composite at the end of the time window, however, the changes are slight for high initial volume fractions. In other words, when the properties of the inclusion increase with respect to the matrix, the time dependency of the properties of the composite increases, however, it tends to be almost constant after a high enough R_{pm}^0. For instance, from the case presented in Fig. 6(c), for a low value of $v_p^0 = 0.1$ the variation of R_{pm}^0 affects $\Delta\bar{R}_{cm}$ even for high values like $R_{pm}^0 = 100$, while for $v_p^0 = 0.5$ and 0.9, the value of $\Delta\bar{R}_{cm}$ is almost

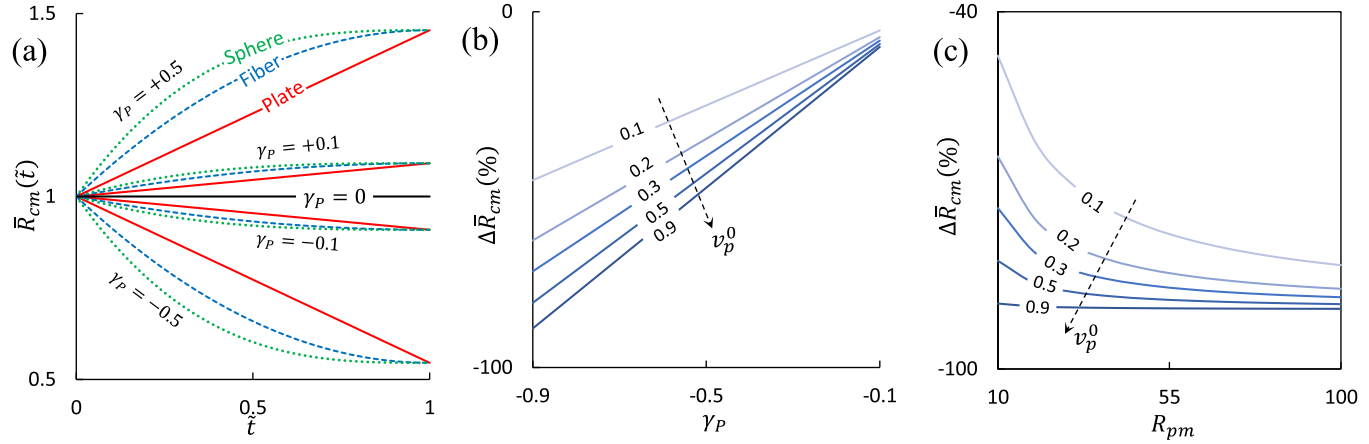

Fig. 6. The parametric study of the normalized reinforcing parameters introduced in Eqs. (26c) and (26d)through the normalized time window, $0 \le \tilde{t} \le 1$ based on the Voigt model in Eq. (22c). (a) The variation of normalized dimensionless reinforcing parameter, $\bar{R}_{cm}(\tilde{t})$, for different types of inclusions, n=1, 2, and 3. Note that for (a) it is assumed that $\beta_P = 0$, $v_p^0 = 0.5$, $\gamma_P' = 0$, and $R_{pm}^0 = 10$. (b) The effect of the efficiency parameter of the inclusion in the interphase, γ_P, and (c) the effect of ratio of properties of the inclusion to the matrix, R_{pm}, on the percent of changes in the normalized parameter at the end of the time window, $\Delta\bar{R}_{cm}$. Note that for (b) and (c) it is assumed that $\beta_P = 0$, $\gamma_P' = 0$, and $\gamma_P = 0.9$ and that $\Delta\bar{R}_{cm}$ is not affected by dissolution dimension, n.

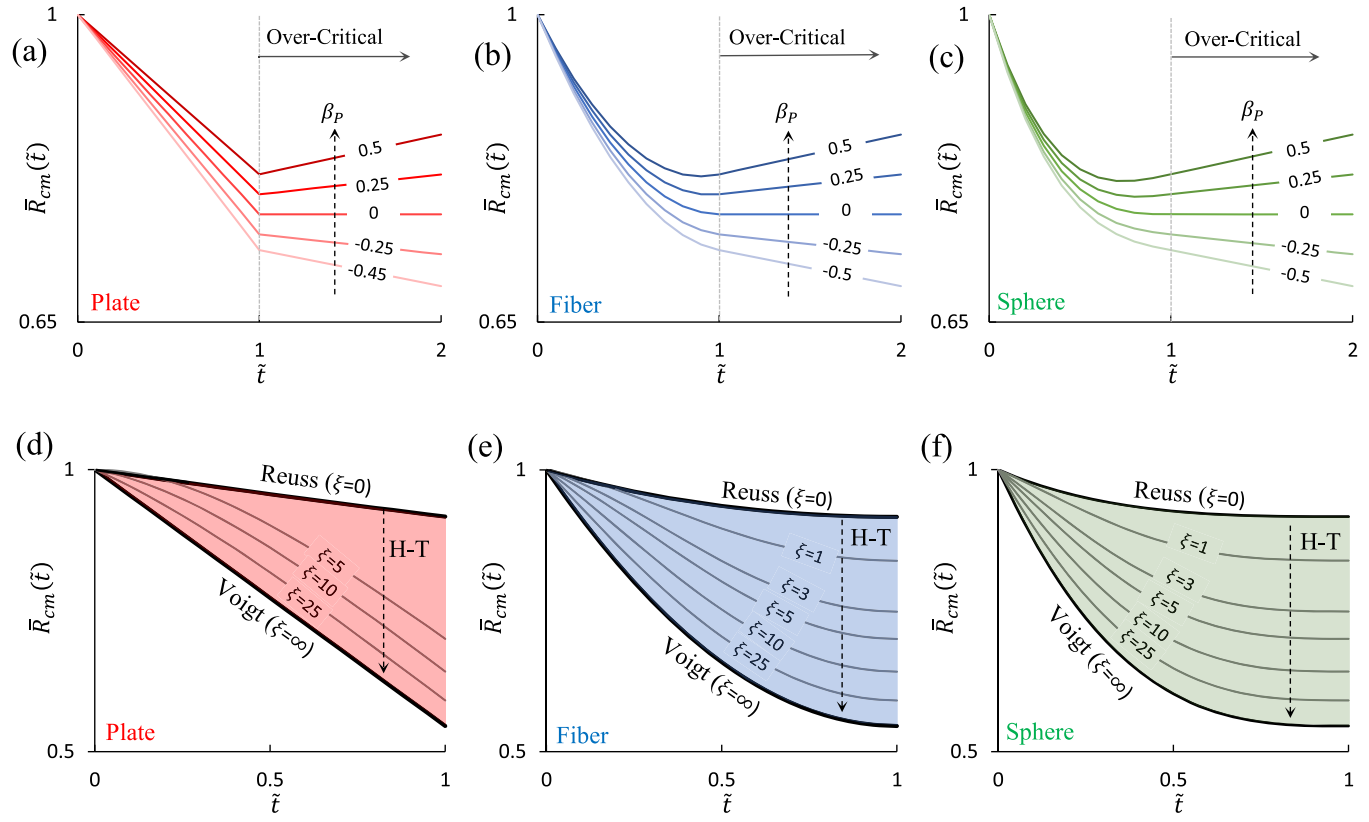

Fig. 7. The variation of normalized dimensionless reinforcing parameter, $\bar{R}_{cm}(\tilde{t})$, with respect to the dimensionless time, $\tilde{t}$. (a) to (c), for a matrix with time-dependent properties based on the Voigt model presented in Eq. (22c) for 1D, 2D, and 3D dissolutions, respectively. Note that for (a) to (c) it is assumed that $v_p^0 = 0.5$, $\gamma_P = -0.25$, $\gamma_P' = 0$, and $R_{pm}^0 = 10$. (d) to (e), the comparison of the three proposed dissolvable micromechanics models (Voigt, Reuss, and H-T) for 1D, 2D, and 3D dissolutions, respectively. Note that for (d) to (e) it is assumed that $v_p^0 = 0.5$, $\gamma_P = -0.5$, $\beta_P = 0$, $\gamma_P' = 0$, and $R_{pm}^0 = 10$.

constant for $R_{pm}^0 > 50$, and $R_{pm}^0 > 20$, respectively.

In Fig. 7(a-c), a matrix with time-dependent properties, $\beta_P \neq 0$, is considered (combined effect of γ_P, and β_P). The initial volume fraction of the inclusion is $v_p^0 = 0.5$, and the efficiency parameter of the inclusion in the interphase is $\gamma_P = -0.25$. It is seen that for negative values of β_P the variation of composite properties with respect to time is strictly descending and there is no extremum, while for $\beta_P > 0$, where γ_P, and β_P behaves opposite, an extremum is observed for all types of inclusions, n. From Eq. (25c), for the plate-like inclusion, extremum happens at $\tilde{t}_{ext} = 1$, while for both fiber- and sphere-likes the extremum is located somewhen $\tilde{t}_{ext} < 1$. For the under-critical, and critical conditions the curves are valid only until $\tilde{t} = 1$, while the over-critical condition is valid until $\tilde{t} = \tilde{t}_m = 2$. It is seen that for all types of inclusions over the time window, $\tilde{t} > 1$, the variation in the properties of the composite is linear since only the time-dependent matrix is in charge which is assumed to vary linearly (see Eq. 19a). This descending-ascending behavior suggests a possibility for optimizing the properties of the composite by proper tuning of the solidification time, however, note that it needs opposite signs for β_P, and γ_P, which is an intrinsic characteristic of the mixture.

The final part of this section compares three different proposed models. From the literature of composite materials, it is proved that the actual elastic constants of composites lie somewhere in the interval between the Voigt and Reuss predictions. Thus, they are respectively the upper and lower bounds of the true value and all the other micromechanics models like H-T locate between them. Unlike the Voigt model which provides a reasonable estimation for some special cases (the longitudinal modulus and the Poisson's ratio of continuous composites), the Reuss model is an inaccurate underestimation. In the meanwhile, the H-T model as a semiempirical equation containing a fitting parameter can fill the gap for predicting the properties of composites. According to the classical 2-phase H-T model, the curve fitting parameter, ξ, is equal to 1, 2, and $2\alpha_p$, for the transverse modulus (continuous inclusions on a square array and discontinuous aligned inclusions), the shear modulus (continuous inclusions on a square array and discontinuous aligned inclusions), and the longitudinal modulus of aligned discontinuous inclusions of the aspect ratio of α_p, respectively [78,11]. It can be shown that $\xi = 0$, converts the H-T model to the Reuss, while with a very large curve fitting parameter, $\xi = \infty$, it reaches the Voigt.

Fig. 7 (d-f) depict the variation of normalized dimensionless reinforcing parameter, $\bar{R}_{cm}(\tilde{t})$, through the normalized time window, $0 \leq \tilde{t} \leq 1$ for different types of inclusions, n=1, 2, and 3, and the effect of the curve fitting parameter of the H-T model, ξ, is investigated. As the effect of all the parameters is studied in detail, to focus on ξ it is assumed that: $\beta_P = 0$, $\gamma_P = -0.5$, $R_{pm}^0 = 10$, and $v_p^0 = 0.5$. It is seen that the direct and inverse rules-of-mixture present far apart graphs and as expected, by increasing ξ the H-T moves from the Reuss to the Voigt. Since increasing ξ is equivalent to higher aspect ratios for the case of discontinuous inclusions, it is concluded that increasing the aspect ratio of inclusions results in higher changes in the properties of the composite with respect to time for all types of inclusions, n.

3.4. Strength of Dissolvable Composites

3.4.1. The 3-phase micromechanics model for strength of composites

Micromechanics models for predicting the strength of composites are more complicated since they should account for different failure mechanisms. The strength of composites is defined as the maximum

stress that can be tolerated at its failure strain. The different load transformation scenarios for continuous and discontinuous composites result in different approaches for the evaluation of the strength. In this section, the study of strength is limited to the case of ultimate tensile strength of dissolvable composites containing continuous inclusions and, therefore sphere-like inclusions, $n = 1$, are not considered. Before establishing the model, it is required to evaluate the strength, $S_i(\widetilde{t})$, and the failure strain, $e_i(\widetilde{t})$, of the interphase as a function of $\widetilde{t}$ from Eqs. (20a) as,

$$S_i(\widetilde{t}) = \widetilde{f}_{ip}(\widetilde{t})(1+\gamma_S)S_p^0 + \widetilde{f}_{im}(\widetilde{t})\left(1+\gamma_S^{'}\right)S_m(\widetilde{t}), \tag{27a}$$

$$e_i(\widetilde{t}) = \widetilde{f}_{ip}(\widetilde{t})(1+\gamma_e)e_p^0 + \widetilde{f}_{im}(\widetilde{t})\left(1+\gamma_S^{'}\right)e_m(\widetilde{t}). \tag{27b}$$

Having the strength and the failure strain of the interphase from Eqs. (27 a-b), a linear approximation for its stress-strain curve with a slope of $S_i(\widetilde{t})/e_i(\widetilde{t})$ can be assumed.

Unlike the micromechanics models for prediction of the elastic constants presented in Section 3.3, where the properties of all the components contribute completely, in the case of strength prediction, the main question that needs to be answered first is: in which strain does the composite fail? In the classical micromechanics models for continuous inclusions, it is acceptable to assume that the failure strain of composite equals the inclusion, because failing in lower strains results in losing the main part of the reinforcing effect of the inclusion. In other words, it is assumed that the matrix in the composite can elongate enough to receive the whole reinforcing potential of the inclusion. This assumption can be inherited by the dissolvable model only for the initial moment, $\widetilde{t} = 0$, since the failure strain of a dissolvable composite, $e_c(\widetilde{t})$, is generally time-dependent. Here, a linear approximation is assumed as,

$$e_c(\widetilde{t}) = \kappa\widetilde{t} + e_p^0, \tag{28a}$$

$$\kappa = \frac{e_c^e - e_p^0}{\widetilde{t}_e}. \tag{28b}$$

It is seen that at the initial moment, $\widetilde{t} = 0$, consisting with the classical (undissolvable and time-independent) models, failure strain of composite is identical to the inclusion, $e_c(\widetilde{t}) = e_p^0$, and at the ending time, $\widetilde{t} = \widetilde{t}_e$, it is equal to the failure strain of a fully interphase composite, $e_c(\widetilde{t}_e) = e_c^e$. The failure strain parameter of the composite, κ, leads the variation of $e_c(\widetilde{t})$ through the dissolution time. Negative values mean that the failure strain of the composite reduces over time, which is not desirable, while positive values enhance the elongation of the composite even higher than the inclusion. Note that, e_c^e, which is required for calculation of κ parameter in Eq. (28b), is in fact the failure strain of the interphase at ending time as composite is fully converted to the interphase. Hence, it can be obtained from Eq. (27b) at $\widetilde{t} = \widetilde{t}_e$ as,

$$e_c^e = v_p^0(1+\gamma_e)e_p^0 + \left(1-v_p^0\right)e_m^e. \tag{28c}$$

The stress equilibrium equation for the dissolvable composites with continuous inclusions is constructed as:

$$\sigma_c(\widetilde{t}) = \sigma_p(\widetilde{t})\widetilde{v}_p(\widetilde{t}) + \sigma_m(\widetilde{t})\widetilde{v}_m(\widetilde{t}) + \sigma_i(\widetilde{t})\widetilde{v}_i(\widetilde{t}). \tag{29a}$$

Then, the strength of the dissolvable composite, $S_c(\widetilde{t})$, can be obtained as the tolerated stress at its failure strain, $e_c(\widetilde{t})$ as,

$$S_c(\widetilde{t}) = S_p\widetilde{v}_p(\widetilde{t}) + S_m\widetilde{v}_m(\widetilde{t}) + S_i\widetilde{v}_i(\widetilde{t}). \tag{29b}$$

The parameters S_p, S_m, and S_i represent the contribution of the inclusion, the matrix, and the interphase in the strength of composite at its failure strain, $e_c(\widetilde{t})$. If the failure strain of the composite, $e_c(\widetilde{t})$, is lower than the failure strain of a component, its contribution in the strength can be evaluated from its stress-strain curve:

$$S_p = \sigma_p^0(e_c(\widetilde{t})), \text{if } e_c(\widetilde{t}) < e_p^0, (\kappa < 0), \tag{30a}$$

$$S_m = \sigma_m(e_c(\widetilde{t}),\ \widetilde{t}), \text{if } e_c(\widetilde{t}) < e_m(\widetilde{t}), \tag{30b}$$

$$S_i = \sigma_i(e_c(\widetilde{t}),\ \widetilde{t}), \text{if } e_c(\widetilde{t}) < e_i(\widetilde{t}). \tag{30c}$$

Fig. 8(a) schematically shows the case that all the components have the failure strain lower than the composite failure strain. Note that, unlike the inclusion, the properties of the matrix and the interphase are generally time-dependent, and therefore, the stress-strain behavior and the strength of the matrix should be evaluated corresponding to the investigated time.

Another scenario is that the failure strain of the composite is higher than that of a component. In this case, it is possible to assume that the component continues its elongation with constant stress equal to its ultimate strength. In other words, it means its original stress-strain curves are modified by adding a horizontal yielding plateau to elongate beyond its failure strain measured individually (see Fig. 8(b)). In this case, the contribution of components in the strength of the composite is simply equal to their strength, and Eq. (30) is replaced by,

$$S_p = S_p^0, \text{if } e_c(\widetilde{t}) \geq e_p^0, (\kappa \geq 0), \tag{31a}$$

$$S_m = S_m(\widetilde{t}), \text{if } e_c(\widetilde{t}) \geq e_i(\widetilde{t}), \tag{31b}$$

$$S_i = S_i(\widetilde{t}), \text{if } e_c(\widetilde{t}) \geq e_m(\widetilde{t}). \tag{31c}$$

Eqs. (31 a-c) impose that a component within a dissolvable composite can stands the strains even higher than the ones that could tolerate individually. This assumption supports the idea that the properties of components tend to be more uniform during the dissolution and diffusion processes.

To simplify the model, it is assumed that the inclusion is linearly elastic, and the matrix and the interphase obey the ideal elastic-plastic behavior and the yielding strain of them is always lower than the failure strain of the composite which is shown graphically in Fig. 8(c). As seen the contribution of the matrix and the interphase is always equal to their strength regardless of the value of the failure strain of composite, however, the inclusion contributes, S_p, treats based on the κ parameter in such a way that for $\kappa \geq 0$ it is identical to the strength of inclusion and for $\kappa < 0$ it linearly decreases. The conclusion for the ideal model is,

$$S_p = S_p^0, \text{if } \kappa \geq 0, \tag{32a}$$

$$S_p = S_p^0\left(1 + \frac{\kappa\widetilde{t}}{e_p^0}\right), \text{if } \kappa < 0, \tag{32b}$$

$$S_m = S_m(\widetilde{t}), \tag{32c}$$

$$S_i = S_i(\widetilde{t}). \tag{32d}$$

Substituting the contributions of the components defined in Eq. (32), the partial volume fractions of the inclusion and the matrix within the interphase from Eq. (18), and the properties of the interphase from Eq. (27a), all into Eq. (29b), the final expression for the strength of the dissolvable composite emerges as,

$$S_c(\widetilde{t}) = S_p^0\left(v_p^0(1+\gamma_s) - \gamma_s\widetilde{v}_p(\widetilde{t})\right) + \left(\beta_s\widetilde{t} + S_m^0\right)\left(\left(1-v_p^0\right) + \gamma_P^{'}\left(\widetilde{v}_p(\widetilde{t}) + \widetilde{v}_i(\widetilde{t}) - v_p^0\right)\right), \text{if } \kappa \geq 0, \tag{33a}$$

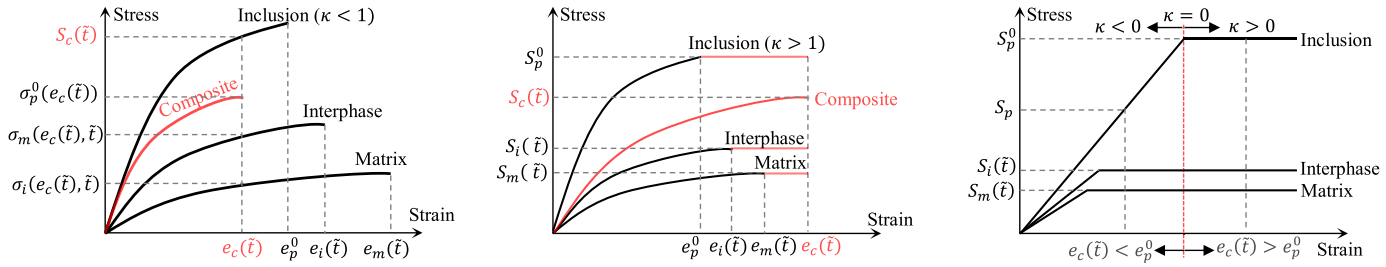

Fig. 8. The schematic of the stress-strain curves of dissolvable composites and their components. the failure strain of the composite is (*a*) lower, (*b*) higher than all the components. (*c*) The schematic of the idealized model.

$$S_c(\tilde{t}) = S_p^0(1+\bar{\kappa}\tilde{t})\left(v_p^0(1+\gamma_s) - \gamma_s \tilde{v}_p(\tilde{t})\right) + \left(\beta_s \tilde{t} + S_m^0\right)\left(\left(1-v_p^0\right) + \gamma_P'\left(\tilde{v}_p(\tilde{t}) + \tilde{v}_i(\tilde{t}) - v_p^0\right)\right), \text{if } \kappa < 0, \tag{33b}$$

where $\bar{\kappa} = (k/e_p^0)$.

3.4.2. *The parametric study on the strength of continuous composites*

It is worth mentioning that in the case of $\kappa \geq 0$, the formulation for the strength of the dissolvable composite in Eq. (33a) is essentially the same as the general expression for the properties of the composite in Eq. (22b) based on the Voigt model, and consequently, all the parametric studies and the conclusions on v_p^0, γ_P, β_P, and $R_{pm}^0 = S_p^0/S_m^0$ parameters presented in the Section 3.3.4 (Figs. 6 and 7) are applicable for the strength. Hence, to prevent duplication, in the following the parametric study is carried out only for the case of $\kappa < 0$ formulated in Eq. (33b). Besides, as the proposed model for prediction strength is developed based on the assumption of continuous inclusions, the sphere-like inclusion, $n = 3$, is set aside, and to be concise, the parametric study is only performed for the fiber-like inclusions, $n = 2$, which are more popular as continuous reinforcements. In Eq. (33b) there are three parameters affecting the strength of the dissolvable composite over time: $\bar{\kappa}$ tunes the contribution of the inclusion in the strength, γ_s reflects the strength efficiency of the dissolved part of the inclusion within the interphase, and

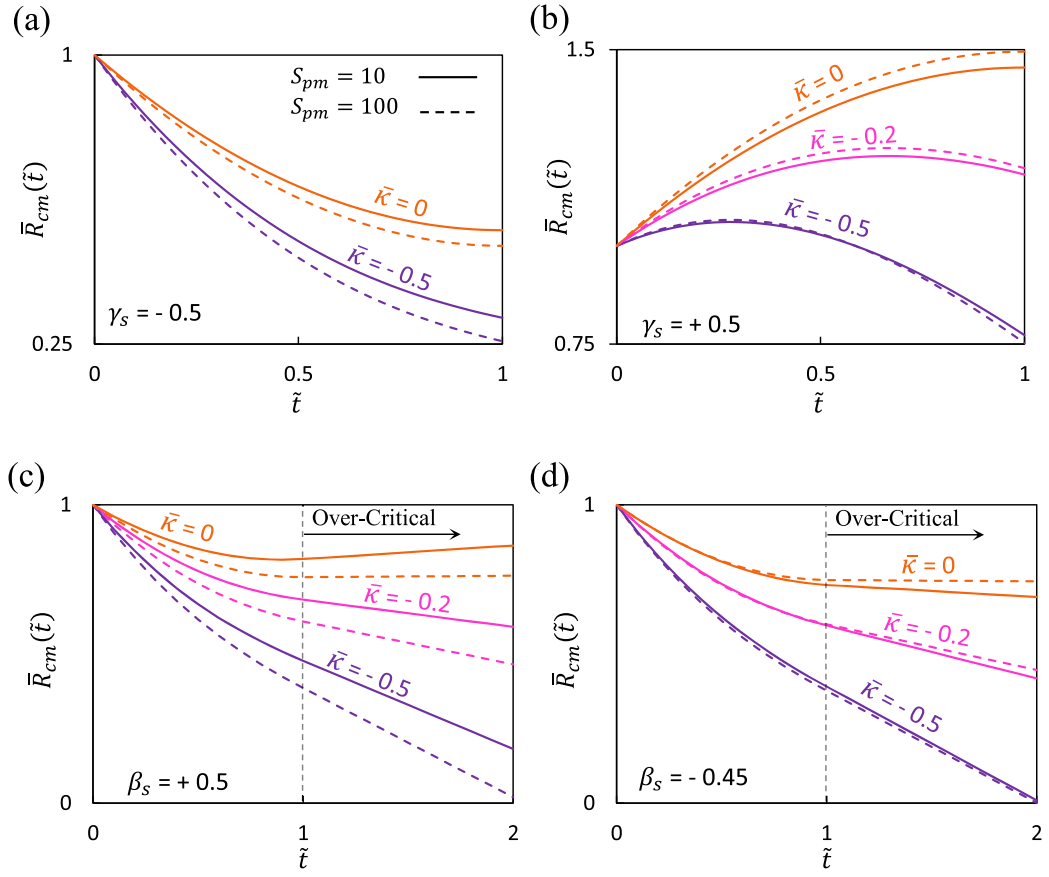

Fig. 9. The effect of contribution parameter of the inclusion in the strength, $\bar{\kappa}$, for the matrix with time-independent strength. (a) and (b), the strength efficiency parameter of inclusion within the interphase, γ_s, is assumed to be negative (-0.5) or positive (+0.5) respectively. (c) and (d), the strength of matrix, increases or decreases over time for $\beta_s = +0.5$ and -0.45, respectively. Note that for (a) to (d) is assumed that $v_p^0 = 0.5$, $\gamma_s' = 0$, $\beta_s = 0$, and $n = 2$.

β_s represents the time-dependent strength of the matrix. The dimensionless parameters of the strength are rewritten as:

$$R^0_{pm} = \frac{S^0_p}{S^0_m}, \text{The ratio of strength of the inclusion to the matrix,} \quad (34a)$$

$$R_{cm}(\widetilde{t}) = \frac{S_c(\widetilde{t})}{S^0_m}, \text{The strength reinforcing parameter of the composite,} \quad (34b)$$

$$\bar{R}_{cm}(\widetilde{t}) = \frac{R_{cm}(\widetilde{t})}{R_{cm}(0)}, \text{The normalized strength reinforcing parameter.} \quad (34c)$$

First, in Fig. 9(a) and (b) it is assumed that the strength of the matrix is constant and time-independent ($\beta_s = 0$) and the variation of normalized dimensionless strength reinforcing parameter, $\bar{R}_{cm}(\widetilde{t})$, through the normalized time window, $0 \le \widetilde{t} \le 1$ for different contribution parameter of the inclusion, $\bar{\kappa}$, is investigated. The initial volume fraction of the fiber-like inclusion, $n = 2$, is assumed $v^0_p = 0.5$, and two different strength ratios of inclusion to the matrix, $R^0_{pm} = 10$, and 100 are considered. From Fig. 9(a) it is seen that when the efficiency parameter of inclusion in the interphase, γ_s, is negative, the normalized strength of the composite reduces over time, and for higher $\bar{\kappa}$ parameter this reduction is higher. It is obvious since $\gamma_s < 0$ means the dissolved part of inclusion presents lower strength compares to the strength of the undissolved part and increasing the values of $\bar{\kappa}$ negatively (remember $\bar{\kappa} < 0$) results in a lower contribution of inclusion in the strength of composite as the failure strain of composite becomes lower than the inclusion. One can see that increasing the inclusion to matrix strength ratio, R^0_{pm}, from 10 to a high ratio of 100 (dash lines), slightly raise the observed reduction in the normalized dimensionless strength, $\bar{R}_{cm}(\widetilde{t})$. It means for stronger inclusions dissolution more affects the strength of composite with respect to its initial condition at $\widetilde{t} = 0$, and it should not be wrongly concluded that the composites with stronger inclusions have lower strength.

In Fig. 9(b), γ_s and $\bar{\kappa}$ behave the opposite as the efficiency parameter is assumed to be positive. It is seen that regarding the values of these two parameters the variation of strength may be strictly ascending or ascending then descending, presenting a maximum value, and the effect of the inclusion to matrix strength ratio, R^0_{pm}, becomes less noticeable when $\bar{\kappa}$ increases. It should be noted that, apart from the present parametric study, in real conditions, the positive efficiency parameter of inclusion for the case of strength seems not to be realistic as $\gamma_s > 0$ means the dissolved part has higher strength than the original unsolved inclusion and consequently the graph presented in Fig. 9(a) may be more realistic.

Finally, Fig. 9(c) and (d) demonstrates the effect of the contribution parameter of the inclusion, $\bar{\kappa}$, for the matrix with time-dependent properties ($\beta \neq 0$). The efficiency parameter of inclusion in the interphase is negative, $\gamma_s = -0.25$, and the initial volume fraction is considered as $v^0_p = 0.5$ and for the over-critical condition, the matrix fading time is $\widetilde{t}_m = 2$. It is seen that in Fig. 9(c) where the strength of matrix increases over time, $\beta_s = 0.5$, the strength of composite may increase even for negative efficiencies, $\gamma_s = -0.25$, however, if the contribution of the inclusion is reduced by $\bar{\kappa}$ parameter, the positive effect of the matrix over the time vanishes. In Fig. 9(d) it is seen that when all the three affecting parameters, γ_s, β_s, and $\bar{\kappa}$ are negative the strength of the composite is strictly descanting, as expected.

4. Implementation of the Dissolvable Micromechanics Model

In this section, the developed micromechanics model is implemented for two case studies of phase transformation due to dissolution. In the first case study, the model is calibrated to the long-term dissolution of fibers in bio-composites exposed to aqueous environments, approximating the observed degradation in the Young's modulus of these composites over a six-month period. In the second case study, the model is fitted to predict the strength degradation due to fiber dissolution in the fabrication process of SPCs.

4.1. Case Study One: Long-Term Dissolution of Fibers in Biocomposites

In this case study, a degradable biocomposites material, introduced in [60], is chosen as an example of a composite subjected to long-term dissolution phase transformation in an aqueous environment. The matrix is composed of degradable polypropylene (PP), which is reinforced by degradable phosphate-based glass fibers of initial diameter, $D^0_p = 47\mu m$, continuously and unidirectionally aligned within the matrix with a mass fraction of 10%. The densities of components are needed to convert the mass fraction to the volume fraction. Since the densities are not reported in [60], a typical density of 2.5 g/cm^3 for glass fibers and 0.9 g/cm^3 for the PP matrix is assumed which results in an initial volume fraction of fibers equal to $v^0_P = 0.0385$. As a continuous fiber reinforced composite (n=2), the time-dependent Young's modulus, $E_c(t)$, of this phase transformed composite under dissolution of fibers can be predicted by Eq. (22b). Before starting dissolution due to exposure to water, at the initial state ($t = 0$), Eq. (22b) turns to a standard 2-phase time-independent Voight equation. Having the initial Young's modulus of matrix, $E^0_m = 522$ MPa, and of the composite, $E_c(0) = 1500$ MPa [60], one can calculate the initial Young's modulus of fiber, $E^0_p = 25.92$ GPa. To proceed through dissolution time frame, it is essential to examine the changes in the volume fraction of fibers with respect to dissolution time. Fig 10(a) presents the experimental measurements for mass loss of the glass fiber over a six-month time interval [60]. Subsequently, the comparison of Eq. (4a) with the measured data reveals that an optimal fit is achieved with an average dissolution rate of $\bar{q} = 0.344\mu m$/month.

Dissolved portion of phosphate-based glass fibers disperses into the surrounding aqueous environment leading to a partial mass loss of composite [60]. Hence, it is logical to consider that the dissolved segment does not contribute to load-bearing, implying an effective property of zero for the dissolved fiber. Referring to Eq. (21a), this condition signifies that the efficiency parameter equals $\gamma_P = -1$.

Given that the composite is fully immersed in the aquatic environment and the dissolved fiber is transferred to the surrounding medium right from the beginning of the examined interval, this suggests a high diffusion rate. This rapid diffusion rate suggests that the whole matrix undergoes the immediate effect of dissolved fiber in a very short initial period. Neglecting this diffusion-evolving period in comparison to the six-month interval under consideration results in the entire matrix undergoing an instantaneous transition into an interphase. In the context of the developed model, the high diffusion rates indicate an exceedingly brief matrix fading time. According to Eq. (6), the matrix fading time, t_m, and the diffusion rate, $\bar{p}$, are inversely proportional and $t_m \to 0$ implies that $\bar{p} \to \infty$. The experimental observations [60], indicating a low dissolution rate and a high diffusion rate, lead to a rate ratio well below its critical threshold, $(\bar{q}/\bar{p}) \ll (\bar{q}/\bar{p})_{crit}$. This implies that the composite remains in a sunder-critical condition throughout the entire investigated interval, exhibiting the characteristics of a two-phase composite comprised of the fibers and an interphase zone. Note that in under-critical condition, the matrix is faded, and its volume fraction is zero. Having the volume fraction of fiber as a function of dissolution time, one can obtain the volume fraction of interphase zone from Eq. (8). As mentioned in [60], the of PP matrix is affected by the diffused fiber products and the aqueous environment. The modification of its Young's modulus over dissolution time takes into account via its efficiency parameter, γ'_P, which is generally a function of dissolution time. Note that since it is assumed that there is no matrix in the composite, the variation of its modulus is also neglected, $\beta_P = 0$. By substituting the experimentally derived parameters into Eq. (22a), one can obtain the Young's modulus of the bio-degradable composite as a function of

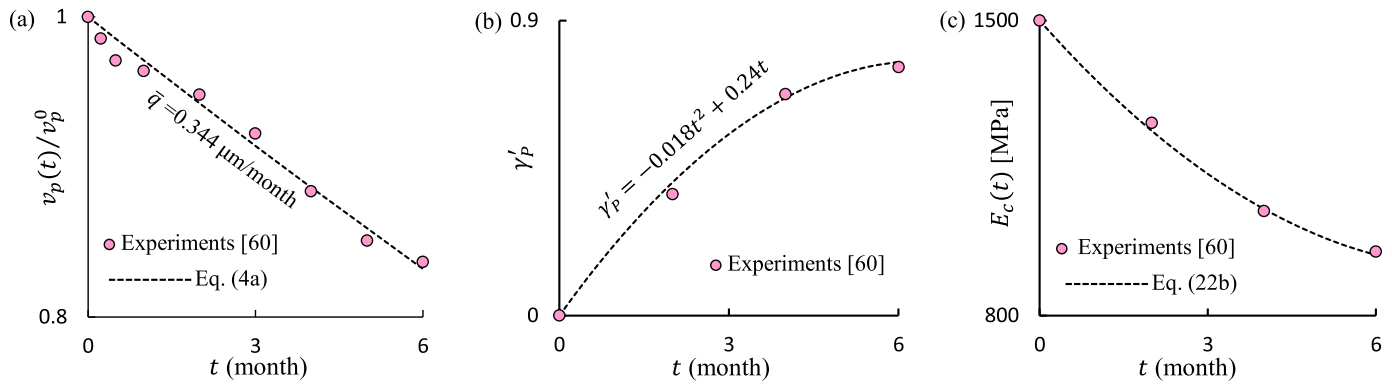

Fig. 10. The calibrated micromechanics model on the long-term dissolution of biocomposites exposed to an aqueous environment. (a) The calibrated dissolution rate of $\bar{q}$ =0.344 μm/month via fitting Eq. (4a) to the measured mass loss of the phosphate-based glass fibers. (b) The calibrated efficiency parameter of the matrix within the interphase zone over the investigated six-month dissolution interval. (c) The comparison between the predicted variation of Young's modulus to the experimentally measured variation [60] over the dissolution interval.

dissolution time. The only undefined parameter is the efficiency parameter, γ_P', which is used as the calibration parameter for fitting to the experiments. Fig. 10(b) depicts the calibrated functionality of as a quadratic polynomial $\gamma_P'(t) = -0.018t^2 + 0.24t$. Finally, Fig. 10(c) compares the calibrated model prediction for Young's modulus with the measured experimental values. It is concluded that the proposed model provides a high level of flexibility, enabling precise calibration and prediction of the degradation effect on properties resulting from dissolution.

4.2. Case Study Two: Short-Term Dissolution of Fibers in SPCs Fabrication

As a case study of short-term dissolution, the proposed micromechanics model has been applied to the experimental measurements of fiber reinforced ($n = 2$) single-polymer composites (SPC) presented in [53] to calibrate the parameters of the model and to demonstrate its capability in predicting the properties of a sample dissolvable SPC composites. The calibration focuses on the tensile strength estimation as the Young's modulus of the component is in the same order of magnitude. Two types of fibers, named T- and W-types with diameters of 0.1 mm and 0.18 mm are laid within the matrix whose annealed properties at the polymerization temperature are listed in Table 2. It is reported that increasing the dosage of the activator accelerates the solidification time. Four different dosages of activator, dose 1 > dose 2 > dose 3 > dose 4 that result in four solidification time, $t_{s1} < t_{s2} < t_{s3} < t_{s4}$, are added to the composite to adjust the level of dissolution of fibers. The corresponding properties of the matrix, and the SPCs made by the two types of fibers, T, and W of the same initial volume fraction of $v_p^0 = 0.15$, are presented in Table 3. In addition, the micrographs of the SPCs associated with the different solidification times are presented in Fig. 11 from [53]. SPCT and SPCW notation corresponds to T- and W-type fibers, respectively.

From Fig. 11(a-d), it is seen that for SPCT type, the provided experimental measurements almost cover whole the dissolution and the diffusion processes as the fiber and the matrix are fully faded at the minimum dosage of activator when the composite is converted to a 1-phase material (see Fig. 11(d)), while it does not happen for SPCW type with the fibers of higher diameter. Besides, the micrographs of SPCW type are only provided for the minimum and the maximum dosages. Hence, the SPCT type composite is selected for the calibration of the dissolvable micromechanics model, and SPCWs measurements remain as the reference for testing the calibrated model. As the first step of calibration, it is essential to attribute the four available experimental measurements of SPCTs to the associated dimensionless times, approximately based on the observation in Fig. 11(a-d): From the end, SPCT-4 can be assumed as the ending time where both the fiber and the inclusion fade, $\tilde{t} = \tilde{t}_m = \tilde{t}_e$, SPCT-3 is considered as the fiber fading time, $\tilde{t} = 1$. As the fading of fiber happens before the interphase, the situation is over-critical (See Fig. 5(c)).

The sample SPCT-2 is somewhen enough far from the milestones and both dissolution and diffusion processes are clearly visible. Finally, the SPCT-1 sample is closest to the initiation of the process, where a narrow hardly visible interphase surrounded the fibers, which is assumed as the initial moment, $\tilde{t} = 0$. Looking in detail at Fig. 11(b), the diameter of the fiber can be approximated as 0.077 mm for the SPCT-2 sample. Given the initial diameter of the T type fiber, $D_p^0 = 0.1$ mm, from Eq. (13a), the corresponding dimensionless solidification time of the SPCT2 sample is calculated as $(\tilde{t}_{s2})_T = 0.23$. Besides, from Fig. 11(b) it is observed that the diameter of the interphase for the SPCT-2 sample is 0.119 mm. Replacing the initial volume fraction of the fibers, $v_p^0 = 0.15$, the solidification time, $(\tilde{t}_{s2})_T = 0.23$, and $n = 2$, one can calculate the matrix fading time, from Eq. (13c) as $(\tilde{t}_m)_T = (\tilde{t}_{s4})_T = 1.91$. It is important to be aware that although the dosage of the activator and consequently the associated solidification times are the same for T, and W fibers, however, the dimensionless solidification times are different because they have different fiber fading times, t_p, due to different initial diameters. From

Table 2
The initial properties of the annealed fibers [53].

Type	Diameter, D_p^0 (mm)	Tensile strength, S_p^0 (MPa)	Failure Strain, e_p^0 (%)
T	0.1	574	24.17
W	0.18	599	25.03

Table 3
The properties of the matrix and the SPCs for different solidification times [53].

Solidification Time	Material Composition	Sample Designation	Tensile strength (MPa)	Failure Strain (%)
dose 1 (t_{s1})	Matrix	M-1	66.51	21.23
	Matrix + T	SPCT-1	94.69	30.03
	Matrix + W	SPCW-1	90.88	28.2
dose 2 (t_{s2})	Matrix	M-2	70.30	20.45
	Matrix + T	SPCT-2	70.57	34.69
	Matrix + W	SPCW-2	76.42	30.59
dose 3 (t_{s3})	Matrix	M-3	74.66	16.70
	Matrix + T	SPCT-3	46.82	41.82
	Matrix + W	SPCW-3	50.07	39.75
dose 4 (t_{s4})	Matrix	M-4	74.79	17.75
	Matrix + T	SPCT-4	32.50	71.64
	Matrix + W	SPCW-4	38.10	46.90

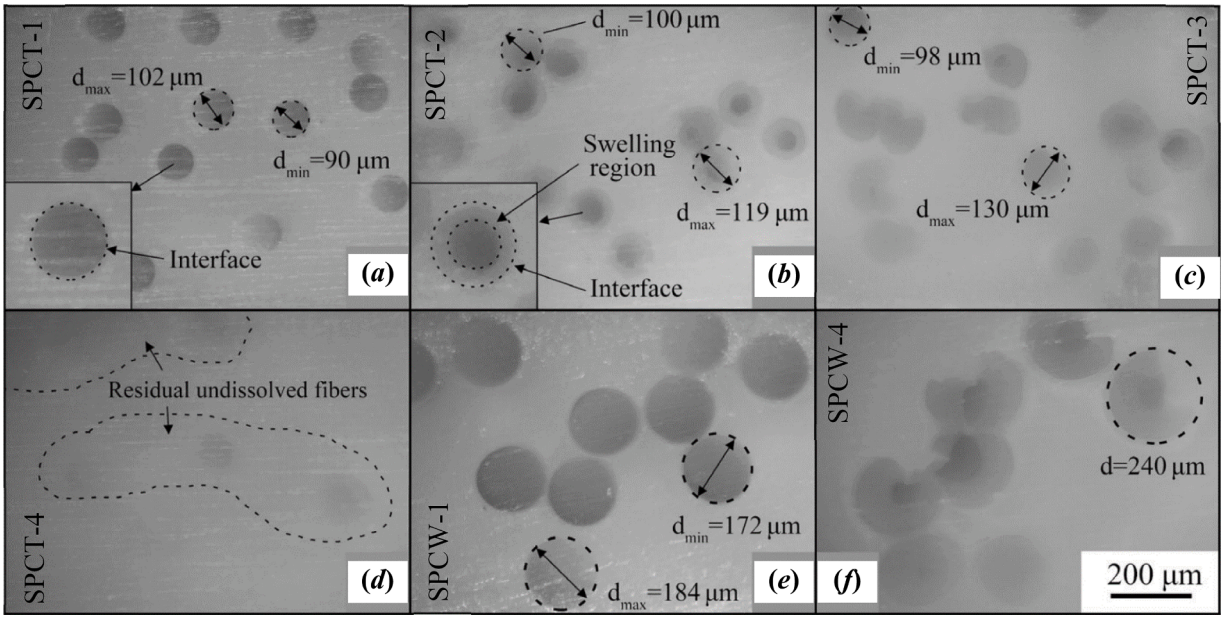

Fig. 11. Microscopy surface topography of SPCs [53]: (*a*) SPCT-1, (*b*) SPCT-2, (*c*) SPCT-3, (*d*) SPCT-4, (*e*) SPCW-1, (*f*) SPCW-4.

Table 4
The calibrated dimensionless solidification time on the experimental data provided in [53].

	SPCTs				SPCWs			
	SPCT-1	SPCT-2	SPCT-3	SPCT-4	SPCW-1	SPCW-2	SPCW-3	SPCW-4
$\widetilde{t}_s$	0	0.23	1	1.91	0	0.128	0.556	1.06

Eq. (5) one can obtain,

$$\frac{(t_p)_W}{(t_p)_T} = \frac{\left(D_p^0\right)_W}{\left(D_p^0\right)_T} = 1.8. \tag{35a}$$

And then from the definition of dimensionless time in Eq. (12a),

$$\frac{(\widetilde{t})_W}{(\widetilde{t})_T} = \frac{(t_p)_T}{(t_p)_W} = \frac{1}{1.8}. \tag{35b}$$

From Eq. (12b), the dimensionless matrix fading time is not related to the initial dimeter and as the initial volume fraction for T, and W fibers is the same, $(\widetilde{t}_m)_W = (\widetilde{t}_m)_T = 1.91$. Table 4 summarizes the calibrated dimensionless solidification times for the eight experimental measurements reported in [53].

Fig. 12(a), depicts the experimental measurements of the strength of the matrix, with respect to time. As the actual processing time corresponding to the activator dosages is not reported, the time-dependent strength of the matrix is mapped to the dimensionless time of the T type fiber, $(\widetilde{t})_T$. The bilinear curve fitting for the strength is also presented and plotted in Fig. 12(a), from which the initial strength of the matrix at $\widetilde{t} = 0$ is $S_m^0 = 67.41$ MPa, and a positive slope of $\beta_s = 7.522$ for $0 < (\widetilde{t})_T < 1$, is fitted followed by a constant strength of 74.91 MPa for $(\widetilde{t})_T > 1$. Note that the presented bilinear approximation can be simply mapped to the dimensionless time of W-type fibers using Eq. (35).

Having the initial strength of the fiber and the matrix, one can predict the initial strength of composites, S_c^0, before starting the dissolution and the diffusion process at $\widetilde{t} = 0$ as a classic composite. Comparing Tables 2, and 3, it is seen that all the SPCs have a failure strain higher than of the fibers which result in a positive contribution parameter of the fiber, $\kappa \geq 0$, which means all the components fully contribute to the strength of composite with their ultimate strength. In this case, the three proposed models in Section 3.3 for the elastic constants are also valid for the strength if the general property of P is replaced by the strength, S. Considering $\widetilde{t} = 0, \widetilde{v}_p(\widetilde{t}) = v_p^0 = 0.15, \widetilde{v}_i(\widetilde{t}) = 0, S_p^0 = 574$ MPa, and $S_m^0 = 67.41$ MPa, the initial strength, S_c^0, of the composite is calculated via Eqs. (22b), and (23b) for the Voigt, and the Resus models as 143.4 MPa, and 77.7 MPa, respectively. Comparing the calculated initial strength with the experimentally measured one for SPCT-1 (94.69 MPa) reveals an overestimation of 51% for the Voigt and an underestimation of 18% for the Reuss model as the upper and lower bounds. Here, it is meaningful to apply the H-T model and calibrate its fitting parameter, ξ, at $\widetilde{t} = 0$ to the strength of SPCT-1. From Eq. (24), $\xi = 2.58$ fits the initial strength predicted by H-T to the experimentally measured strength of SPCT-1. The fitted H-T model is selected for the next steps of calibration of the model. Now, Eq. (24) with $\xi = 2.58$ is evaluated for the rest $(\widetilde{t})_T =$ 0.22, 1, and 1.91 listed in Table 3 to look for the efficiency parameters that match the corresponding measured strengths in Table 3 for SPCT-2, SPCT-3, and SPCT-4 samples. Note that the efficiency parameters of the fiber, γ_s, and the matrix, γ_s', that reflect the quality of them within the interphase zone, are implicitly introduced in Eq. (24) as the strength of interphase, defined in Eqs. (20 c-d), and (21). Lacking detailed investigations on the strength of interphase, it is assumed that the efficiency parameter of the fiber and the matrix are the same, $\gamma_s = \gamma_s'$. The calibrated efficiency parameters, with respect to the dimensionless time of the T type fiber, $(\widetilde{t})_T$, are shown in Fig. 12(b). It is seen that the efficiency parameter is not constant and for the provided experiments in [53], it increases over the dimensionless time. Fitting the efficiency parameter, the calibration of the proposed micromechanics model is completed.

Fig. 12(c) and (d) demonstrate the predicted strength by the three proposed models for T-type, and W-types SPCs, respectively. The calibrated efficiency parameter in Fig. 12(b) is applied to all the models, and the fitting parameter of the H-T model is assumed $\xi = 2.58$. Since the

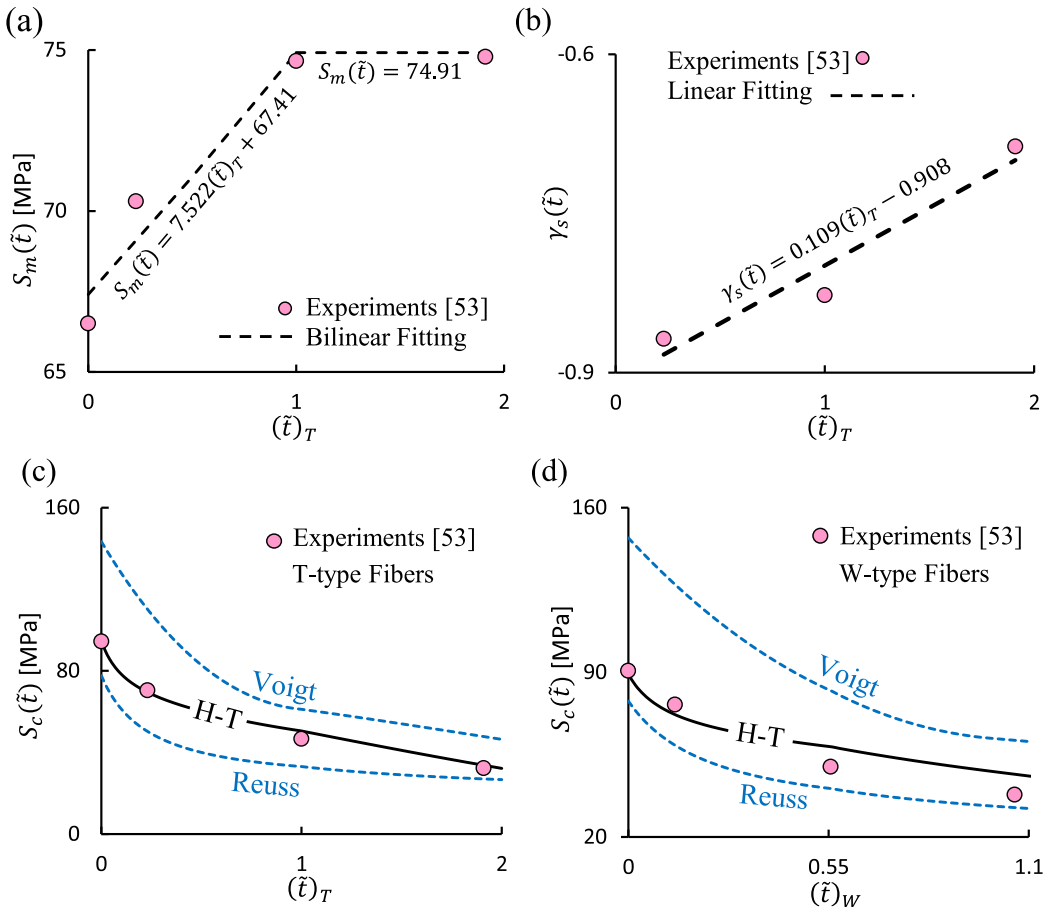

Fig. 12. The calibrated micromechanics model on the short-term dissolution and diffusion of fibers in fabrication of SPCs. (a) The variation of the strength of the matrix with respect to dimensionless time of the T-type fibers. Note: The time-dependent properties of the matrix can be mapped to the dimensionless time of the W-type fibers via Eq. (35). (b) Calibrated efficiency parameter of the fiber and the matrix within the interphase, $\gamma_s = \gamma_s'$, versus the dimensionless time of the T-type fibers. (c) and (d), the comparison of the strength predicted by the proposed dissolvable micromechanics model with the experiments for T-type and W-type fibers, respectively.

efficiency parameter is calibrated using the experimental data of SPCTs, it is seen in Fig. 12(c) that the prediction by the H-T model fits perfectly the experiments as expected, and the Voigt and the Reuss models act as the upper and lower limits. To test the capability of the proposed calibrated model, the prediction of strength for W-type SPCs versus its dimensionless time, $(\tilde{t})_W$, are presented in Fig. 12(d) and compared to the experimental data in [53]. The strength of matrix presented in Fig. 12(a) is mapped to $(\tilde{t})_W$ using Eq. 35(b) as,

$$S_m(\tilde{t}) = 13.54(\tilde{t})_W + 67.41. \tag{36a}$$

The calibrated efficiency parameter of T-type SPCs, are used for W-types as the fiber and the matrix are essentially the same materials, and assuming the same dissolution and diffusion processes, the quality of portions of matrix and the fiber within the interphase zone is the same for T- and W-type SPCs:

$$\gamma_s(\tilde{t}) = 0.109(\tilde{t})_W - 0.908. \tag{36b}$$

Compared to the experimental data, one can observe that the proposed model is able to predict the decreasing trend of strength through the dissolution time with reasonable accuracy for the set of experimental data of W-type SPCs. It is noted that for the provided data in [53], the strength of both T- and W- SPCs for a low dosage of the activator is significantly lower than the pure matrix with the same dosage (from Table 3, dose 3 around 35%, and dose 4 around 50%). It means the interphase zone is remarkably weaker than the matrix, which is reflected to the model as the negative efficiency parameter, γ_s.

5. Conclusion

In conclusion, this study introduces a novel micromechanics model tailored to predict the evolving properties of composites experiencing the gradual dissolution of reinforcing inclusions as a phase transformation problem, leading to the formation of an interphase zone comprising the diffused dissolved portion within the matrix. A thorough dimensionless parametric investigation is conducted to elucidate the impact of all parameters introduced in the model. The proposed model can be used in various situations, including predicting properties during the manufacturing of SPCs and dealing with long-term dissolution in different conditions, such as industrial or biological settings, as demonstrated in the case studies. The key considerations, limitations and findings drawn from the developed model can be outlined as follows:

- **Effect of inclusion shape in dissolution:** As a novelty, by introducing the dissolution dimension (1D for plate-like, 2D for fiber-like, and 3D for spherical-like inclusions), the model is able to consider the influence of inclusion shape on the variation of volume fraction over the dissolution time. While the presented analytical model provides a simple yet effective approach with a sufficient degree of freedom for predicting the observed experimental behavior in composites due to phase transformation, the use of the model requires having an assessment of the average dissolution and diffusion rates.

- **Efficiency of properties within the interphase:** Two efficiency parameters have been introduced for the dissolved portion of inclusion and the diffusion-affected portion of the matrix. These two parameters reflect the quality of these two components of the interphase zone, comparing their virgin properties before dissolution and diffusion. As illustrated in case studies, these parameters can be effectively utilized as fitting parameters for calibrating the model according to experimental results.
- **Semi-Empirical Fitting Parameter:** In cases where basic models of direct and inverse rule-of-mixture (Voigt and Reuss models) fail to accurately predict the observed experimental behavior, the modified Halpin-Tsai equation, due to its intrinsic fitting parameter resulting from its semi-empirical nature, can serve as a calibration parameter. This fitting parameter dependents on the aspect ratio and packing of the inclusion and can be utilized as a superior means of adjustment to implicitly take into account the shape of inclusions from reinforcement perspective.
- **Effect of temperature:** While the effect of temperature on the phase transformation process due to dissolution is not explicitly outlined in the presented model, this influence can be implicitly considered by temperature-dependent dissolution and diffusion rates, or by incorporating a temperature-dependent function for the properties and efficiencies of the inclusion and matrix within the model.
- **Model Implementation:** The numerical implementation of the proposed model is straightforward due to its analytical closed-form nature. This feature makes it inherently efficient for both calibration and prediction processes. The simplicity of the model allows for low computational costs, especially when the necessary inputs for calibration are provided.
- **Limitations:** Through the development of the model, we have overcome the limitations of classical models by incorporating time-dependent variations in volume fractions and considering scenarios of interphase growth. Constructing the evolving interphase involves the development of a time-dependent three-phase model, rooted in three established classical micromechanical approaches, the Voigt, the Reuss, and the semiempirical Halpin-Tsai equation. It is imperative to recognize that the model introduced herein is not equipped to foresee certain phenomena, including interfacial shear strength, weakened bond or debonding between the inclusion and the matrix. This limitation stems from fundamental simplifications inherent in the chosen classical model as its foundation, however, the established model incorporates the failure of the interphase zone by offering an indirect means of controlling the interphase performance throughout the phase-transformation process by adjusting the efficiency parameters of dissolved fiber and under-diffusion matrix within the interface. Nonetheless, it is crucial to differentiate between phase transformation in the form of dissolution, usually induced by elevated temperatures, and progressive degradation resulting from adverse environmental conditions, such as corrosion. In dissolution, improved bonding between the inclusion and the matrix might occur, whereas, in the case of the latter, the effect is often the opposite. In future investigations, the authors have planned the ongoing refinement and extension of the proposed model to systematically address and overcome the acknowledged limitations.

In summary, the developed model not only provides a valuable tool for predicting the behavior of composites during phase transformation but also serves as a foundation for further advancements in understanding and optimizing composite materials. Its simplicity, versatility, and potential for calibration make it a promising asset for researchers and practitioners in the composite community seeking accurate predictions and insights into the complex interplay of phase transformations.

CRediT authorship contribution statement

S.K. Jalali: Conceptualization, Formal analysis, Methodology, Software, Validation, Visualization, Writing – original draft. **N.M. Pugno:** Conceptualization, Formal analysis, Funding acquisition, Methodology, Supervision, Writing – review & editing.

Declaration of competing interest

The authors declare that they have no known competing financial interests or personal relationships that could have appeared to influence the work reported in this paper.

Data availability

No data was used for the research described in the article.

References

[1] Fang H, Bai Y, Liu W, Qi Y, Wang J. Connections and structural applications of fibre reinforced polymer composites for civil infrastructure in aggressive environments. Compos Part B Eng 2019;164:129–43. https://doi.org/10.1016/j.compositesb.2018.11.047.
[2] Tomar SS, Zafar S, Talha M, Gao W. State of the art of composite structures in non-deterministic framework: A review. Thin-Walled Struct 2018;132:700–16. https://doi.org/10.1016/j.tws.2018.09.016.
[3] Chandrathilaka ERK, Kristombu Baduge S, Mendis P, Thilakarathna PSM. Structural applications of synthetic fibre reinforced cementitious composites: A review on material properties, fire behaviour, durability and structural performance. Structures 2021;34:550–74. https://doi.org/10.1016/j.istruc.2021.07.090.
[4] Lin K, et al. Dynamic strength, reinforcing mechanism and damage of ceramic metal composites. Int J Mech Sci 2022;213:107580. https://doi.org/10.1016/j.ijmecsci.2022.107580.
[5] Li L, et al. A database construction method for data-driven computational mechanics of composites. Int J Mech Sci 2023;249:108232. https://doi.org/10.1016/j.ijmecsci.2023.108232.
[6] Tang S, Design Hu C. Preparation and Properties of Carbon Fiber Reinforced Ultra-High Temperature Ceramic Composites for Aerospace Applications: A Review. J Mater Sci Technol 2016;33:117–30. https://doi.org/10.1016/j.jmst.2016.08.004.
[7] Tang S, Ch Hu. Design, Preparation and Properties of Carbon Fiber Reinforced Ultra-High Temperature Ceramic Composites for Aerospace Applications: A Review. J Mater Sci Technol 2017;33(2):117–30. https://doi.org/10.1016/j.jmst.2016.08.004.
[8] Cho K, Rajan G, Farrar P, Prentice L, Gangadhara Prusty B. Dental resin composites: A review on materials to product realizations. Compos Part B 2022;230. https://doi.org/10.1016/j.compositesb.2021.109495.
[9] Ikumapayi OM, et al. Ceramics matrix composites for biomedical applications - a review. Mater Today. Proc 2023. https://doi.org/10.1016/j.matpr.2023.08.168.
[10] Griffits AA. The phenomena of rupture and flow in solids. Philos Trans R Soc 1920;221:163–98. https://doi.org/10.1098/rsta.1921.0006.
[11] Raju B, Hiremath SR, Mahapatra DR. A review of micromechanics based models for effective elastic properties of reinforced polymer matrix composites. Compos Struct 2018;204:607–19. https://doi.org/10.1016/j.compstruct.2018.07.125.
[12] Lavagna L, Massella D, Pantano MF, Bosia F, Pugno NM, Pavese M. Grafting carbon nanotubes onto carbon fibres doubles their effective strength and the toughness of the composite. Compos Sci Technol 2018;166:140–9. https://doi.org/10.1016/j.compscitech.2018.03.015.
[13] Valentini L, Bittolo Bon S, Pugno NM, Hernandez Santana M, Lopez-Manchado MA, Giorgi G. Synergistic icephobic behaviour of swollen nitrile butadiene rubber graphene and/or carbon nanotube composites. Compos Part B Eng 2019;166:352–60. https://doi.org/10.1016/j.compositesb.2018.11.095.
[14] Valentini L, Bittolo Bon S, Pugno NM. Graphene and Carbon Nanotube Auxetic Rubber Bionic Composites with Negative Variation of the Electrical Resistance and Comparison with Their Nonbionic Counterparts. Adv Funct Mater 2017;27. https://doi.org/10.1002/adfm.201606526.
[15] Wan L, Ismail Y, Sheng Y, Ye J, Yang D. A review on micromechanical modelling of progressive failure in unidirectional fibre-reinforced composites. Compos. C: Open Access 2023;10:100348. https://doi.org/10.1016/j.jcomc.2023.100348.
[16] Gopinath G, Batra RC. A common framework for three micromechanics approaches to analyze elasto-plastic deformations of fiber-reinforced composites. Int J Mech Sci 2018;148:540–53. https://doi.org/10.1016/j.ijmecsci.2018.09.003.
[17] Zheng-Ming H, Chun-Chun Z, Yuan-De X. Stiffness prediction of short fiber reinforced composites. Int J Mech Sci 2019;161-162:105068. https://doi.org/10.1016/j.ijmecsci.2019.105068.
[18] Kathavate VS, Pawar DN, Bagal NS, Adkine AS, Salunkhe VG. Micromechanics Based Models for Effective Evaluation of Elastic Properties of Reinforced Polymer

Matrix Composites. Mater Today. Proc 2020;21(2):1298–302. https://doi.org/10.1016/j.matpr.2020.01.166.
[19] Li J, Qiu J, Weng J, Yang EH. Micromechanics of engineered cementitious composites (ECC): A critical review and new insights. Constr Build Mater 2023; 362:129765. https://doi.org/10.1016/j.conbuildmat.2022.129765.
[20] Hill R. The elastic behaviour of a crystalline aggregate. Proc Phys Soc Sect A 1952; 65:349–54. https://doi.org/10.1088/0370-1298/65/5/307.
[21] Hashin Z, Shtrikman S. A variational approach to the theory of the elastic behaviour of multiphase materials 1963;11.
[22] Nanoth R, Jayanarayanan K, Kumar PS, Balachandran M, Pegoretti A. Static and dynamic mechanical properties of hybrid polymer composites: A comprehensive review of experimental, micromechanical and simulation approaches. Compos. - A: Appl. Sci. 2023;174:107741. https://doi.org/10.1016/j.compositesa.2023.107741.
[23] Wang Y, Zh Huang. A Review of Analytical Micromechanics Models on Composite Elastoplastic Behaviour. Procedia Eng 2017;173:1283–90.
[24] Budiansky B. On the elastic moduli of some heterogeneous materials. J Mech Phys Solids 1965;13:223–7. https://doi.org/10.1016/0022-5096(65)90011-6.
[25] Hill R. A self-consistent mechanics of composite materials. J Mech Phys Solids 1965;13:213–22. https://doi.org/10.1016/0022-5096(65)90010-4.
[26] Christensen RM, Lo KN. Solutions for Effective Shear Properties in Three Phase Sphere and Cylinder Models. J Mech Phys Solids 1979;27:315–30.
[27] Huang Y, Hu KX, Chandra A. A generalized self-consistent mechanics method for composite materials with multiple inclusions. J Mech Phys Solids 1994;42: 491–504. https://doi.org/10.1016/0022-5096(94)90035-3.
[28] Mori T, Tanaka K. Average stress in matrix and average elastic energy of materials with misfitting inclusions. Acta Metall 1973;21:571–4. https://doi.org/10.1016/0001-6160(73)90064-3.
[29] Halpin J, Tsai S. Effects of Environmental Factors on Composite Materials. Air Force Tech Rep AFML-TR 1969:67–423.
[30] Jones Robert M. Mechanics of Composite Materials. 2nd ed., 4. Boca Raton: CRC Press; 1999.
[31] Lu K, Wang Z, Li G, Jiang R, Sui G, Yang X, et al. Enhanced longitudinal compressive strength of CFRP composites through matrix stiffening via flexible/rigid epoxide grafted silica: A combined analysis of simulation and experiments. Compos Part B Eng 2022;235:109756. https://doi.org/10.1016/j.compositesb.2022.109756.
[32] Wu YP, Jia QX, Yu DS, Zhang LQ. Modeling Young's modulus of rubber-clay nanocomposites using composite theories. Polym Test 2004;23:903–9. https://doi.org/10.1016/j.polymertesting.2004.05.004.
[33] Ku H, Wang H, Pattarachaiyakoop N, Trada M. A review on the tensile properties of natural fiber reinforced polymer composites. Compos Part B Eng 2011;42:856–73. https://doi.org/10.1016/j.compositesb.2011.01.010.
[34] Asgharian H, Baniasadi E. A review on modeling and simulation of solar energy storage systems based on phase change materials. J Energy Storage 2019;21: 186–201. https://doi.org/10.1016/j.est.2018.11.025.
[35] Xiaoqing L, Peng Y, Renqiang L, Hui J, Xiaoyan L. A novel model for calculating the melting process of composite phase change materials. J Energy Storage 2020;30: 101504. https://doi.org/10.1016/j.est.2020.101504.
[36] Sattari H, Mohebbi A, Afsahi MM, Azimi Yancheshme A. CFD simulation of melting process of phase change materials (PCMs) in a spherical capsule. Int J Refrig Int J Refrig 2017;73:209–18.
[37] Qi Ge, et al. Thermomechanical behavior of shape memory elastomeric composites. J Mech Phys Solids 2012;60(1):67–83. https://doi.org/10.1016/j.jmps.2011.09.011.
[38] Luo X, Mather PT. Preparation and Characterization of Shape Memory Elastomeric Composites. Macromolecules 2009;42(19):7251–3. https://doi.org/10.1021/ma9015888.
[39] Ge Q, Serjouei A, Qi HJ, Dunn ML. Thermomechanics of printed anisotropic shape memory elastomeric composites. Int J Solids Struct 2016;102-103:186–99.
[40] Bellah M, Nosonovsky M, Rohatgi P. Shape Memory Alloy Reinforced Self-Healing Metal Matrix Composites. Appl Sci 2023;13(12):6884. https://doi.org/10.3390/app13126884.
[41] Marfia S. Micro–macro analysis of shape memory alloy composites. Int J Solids Struct 2005;42(13):3677–99. https://doi.org/10.1016/j.ijsolstr.2004.11.020.
[42] Tsoi KA, Stalmans Schrooten J. Transformational behaviour of constrained shape memory alloys. Acta Mater 2002;50(14):3533–44. https://doi.org/10.1016/S1359-6454(02)00145-3.
[43] Dorigato A, Pegoretti A. Biodegradable single-polymer composites from polyvinyl alcohol. Colloid Polym Sci 2012;290:359–70. https://doi.org/10.1007/s00396-011-2556-z.
[44] Matabola KP, De Vries AR, Moolman FS, Luyt AS. Single polymer composites: A review. J Mater Sci 2009;44:6213–22. https://doi.org/10.1007/s10853-009-3792-1.
[45] Karger-Kocsis J, Bárány T. Single-polymer composites (SPCs): Status and future trends. Compos Sci Technol 2014;92:77–94. https://doi.org/10.1016/j.compscitech.2013.12.006.
[46] Kmetty Á, Bárány T, Karger-Kocsis J. Self-reinforced polymeric materials: A review. Prog Polym Sci 2010;35:1288–310. https://doi.org/10.1016/j.progpolymsci.2010.07.002.
[47] Gong Y, Liu A, Yang G. Polyamide single polymer composites prepared via in situ anionic polymerization of ε-caprolactam. Compos Part A Appl Sci Manuf 2010;41: 1006–11. https://doi.org/10.1016/j.compositesa.2010.04.006.
[48] Barkoula NM, Peijs T, Schimanski T, Loos J. Processing of single polymer composites using the concept of constrained fibers. Polym Compos 2005;26: 114–20. https://doi.org/10.1002/pc.20082.
[49] Teishev A, Marom G. The effect of transcrystallinity on the transverse mechanical properties of single-polymer polyethylene composites. J Appl Polym Sci 1995;56: 959–66. https://doi.org/10.1002/app.1995.070560809.
[50] Dencheva N, Denchev Z, Pouzada AS, Sampaio AS, Rocha AM. Structure-properties relationship in single polymer composites based on polyamide 6 prepared by in-mold anionic polymerization. J Mater Sci 2013;48:7260–73. https://doi.org/10.1007/s10853-013-7546-8.
[51] Kestenbach H-J, Loos J, Petermann J. Transcrystallization at the interface of polyethylene single-polymer composites. Mater Res 1999;2:261–9. https://doi.org/10.1590/s1516-14391999000400005.
[52] Tohidia SD, Rochaa AM, Engesserc B, Denchevab NV, Denchev Z. Micromechanical finite element parametric study of polyamide 6 based single polymer composites reinforced by woven textile structures. Compos Struct 2019;225:111088. https://doi.org/10.1016/j.compstruct.2019.111088.
[53] Song L, Wang X, Xie P, Ding Y, Dang K, Yang W. Dissolution window in in situ polymerization preparation of polyamide single-polymer composites. Polym Eng Sci 2021;61:1662–72. https://doi.org/10.1002/pen.25690.
[54] Zhao Y, Yu J, Jin W. Damage analysis and cracking model of reinforced concrete structures with rebar corrosion. Corros Sci 2011;53:3388–97. https://doi.org/10.1016/j.corsci.2011.06.018.
[55] Lu C, Jin W, Liu R. Reinforcement corrosion-induced cover cracking and its time prediction for reinforced concrete structures. Corros Sci 2011;53:1337–47. https://doi.org/10.1016/j.corsci.2010.12.026.
[56] Wong HS, Zhao YX, Karimi AR, Buenfeld NR, Jin WL. On the penetration of corrosion products from reinforcing steel into concrete due to chloride-induced corrosion. Corros Sci 2010;52:2469–80. https://doi.org/10.1016/j.corsci.2010.03.025.
[57] Prian L, Barkatt A. Degradation mechanism of fiber-reinforced plastics and its implications to prediction of long-term behavior. J Mater Sci 1999;34:3977–89. https://doi.org/10.1023/A:1004647511910.
[58] Krauklis AE, Echtermeyer AT. Dissolving Cylinder Zero-Order Kinetic Model for Predicting Hygrothermal Aging of Glass Fiber Bundles and Fiber-Reinforced Composites. Int Glas Fiber Symp 2018. 2018.
[59] Krauklis Andrey E, ATE Abedin IGagani. Long-Term Hydrolytic Degradation of the Sizing-Rich Composite Interphase. Coating 2019;9:263. https://doi.org/10.3390/coatings9040263.
[60] Khan RA, Khan MA, Sultana S, Nuruzzaman Khan M, Shubhra QTH, Noor FG. Mechanical, degradation, and interfacial properties of synthetic degradable fiber reinforced polypropylene composites. J Reinf Plast Compos 2010;29:466–76. https://doi.org/10.1177/0731684408100699.
[61] Lehtonen TJ, Tuominen JU, Hiekkanen E. Resorbable composites with bioresorbable glass fibers for load-bearing applications. in vitro degradation and degradation mechanism. Acta Biomater 2013;9:4868–77. https://doi.org/10.1016/j.actbio.2012.08.052.
[62] Att W, Hori N, Takeuchi M, Ouyang J, Yang Y, Anpo M, et al. Time-dependent degradation of titanium osteoconductivity: An implication of biological aging of implant materials. Biomaterials 2009;30:5352–63. https://doi.org/10.1016/j.biomaterials.2009.06.040.
[63] Dziuba D, Meyer-Lindenberg A, Seitz JM, Waizy H, Angrisani N, Reifenrath J. Long-term in vivo degradation behaviour and biocompatibility of the magnesium alloy ZEK100 for use as a biodegradable bone implant. Acta Biomater 2013;9: 8548–60. https://doi.org/10.1016/j.actbio.2012.08.028.
[64] Witte F, Kaese V, Haferkamp H, Switzer E, Meyer-Lindenberg A, Wirth CJ, et al. In vivo corrosion of four magnesium alloys and the associated bone response. Biomaterials 2005;26:3557–63. https://doi.org/10.1016/j.biomaterials.2004.09.049.
[65] Peuster M, Beerbaum P, Bach FW, Hauser H. Are resorbable implants about to become a reality? Cardiol Young 2006;16:107–16. https://doi.org/10.1017/S1047951106000011.
[66] Zberg Bruno, Peter J, Uggowitzer JFL. MgZnCa glasses without clinically observable hydrogen evolution for biodegradable implants. Nat Mater 2009;8: 887–91. https://doi.org/10.1038/nmat2542. Epub 2009 Sep 27.
[67] Witte F, Fischer J, Nellesen J, Crostack HA, Kaese V, Pisch A, et al. In vitro and in vivo corrosion measurements of magnesium alloys. Biomaterials 2006;27:1013–8. https://doi.org/10.1016/j.biomaterials.2005.07.037.
[68] Zhang E, Xu L, Yu G, Pan F, Yang K. In vivo evaluation of biodegradable magnesium alloy bone implant in the first 6 months implantation. J Biomed Mater Res A 2009;90:882–93. https://doi.org/10.1002/jbm.a.32132.
[69] Hermann A, Shojaei A, Dirk Steglich, Höche D, c Zeller-Plumhoff Berit, Cyron CJ. Combining peridynamic and finite element simulations to capture the corrosion of degradable bone implants and to predict their residual strength. Int J Mech Sci 2022;220:107143.
[70] Zhang Q, Zhao Z, Wu D, Chen K, Weng S. Mechanics-guided design of inflatable heterogeneous shape memory polymer vascular stents. Int J Mech Sci 2023;254: 108405. https://doi.org/10.1016/j.ijmecsci.2023.108405.
[71] Staiger MP, Pietak AM, Huadmai J, Dias G. Magnesium and its alloys as orthopedic biomaterials: A review. Biomater 2006;27(9):1728–34. https://doi.org/10.1016/j.biomaterials.2005.10.003.
[72] Chandra G, Pandey A. Biodegradable bone implants in orthopedic applications: a review. Biocybern Biomed Eng 2020;40(2):596–610.
[73] Romanovskaia EM, Mityushov EA, Berestova SA, Romanovskaia ND. Modeling of microstructural stresses of composite materials during phase transformations. AIP Conf. Proc. 2020;2293:120011. https://doi.org/10.1063/5.0031296.
[74] Marfia S, Sacco E. Micromechanics and Homogenization of SMA-Wire-Reinforced Materials. J Appl Mech 2005;72(2):259–68. https://doi.org/10.1115/1.1839186.

[75] Zhang Y, Yang K, Zhao XY. An Eshelbian Homogenization Solution for the Coupled Mechanical-Diffusion Problem. Mech Solids 2023;58:1410–36. https://doi.org/10.3103/S0025654423600332.
[76] Xu B, Wei A, Ye J, Sha W, Guo F. Transverse creep induced by interfacial diffusion in fiber-reinforced composites: A micromechanics model and computational validation. Int J Mech Sci 2022;213:106877. https://doi.org/10.1016/j.ijmecsci.2021.106877.
[77] Pan HH, Weng GJ. Thermal stress and volume change during a cooling process involving phase transformation. J Therm Stress 1992;15(1):1–23. https://doi.org/10.1080/01495739208946117.
[78] Gibson RF. Principal of composite material mechanics. 4th ed., 53. CRC Press; 2016.
[79] Tandon GP, Weng GJ. Average stress in the matrix and effective moduli of randomly oriented composites. Compos Sci Technol 1986;27:111–32. https://doi.org/10.1016/0266-3538(86)90067-9.
[80] Xu Z, Shao X, Huang Q. A micromechanical model of multi-scale nano-reinforced composites. Polym Test 2023;125:108121. https://doi.org/10.1016/j.polymertesting.2023.108121.